*J. Fluid Mech.* (2010), *vol.* 660, *pp.* 5–36.  
doi:10.1017/S0022112010002831

# The evaporatively driven cloud-top mixing layer

JUAN PEDRO MELLADO†

Institut für Technische Verbrennung, RWTH Aachen University, Templergraben 64, 52056 Aachen, Germany

(Received 29 October 2009; revised 12 May 2010; accepted 12 May 2010; first published online 27 July 2010)

Direct numerical simulations of the turbulent temporally evolving cloud-top mixing layer are used to investigate the role of evaporative cooling by isobaric mixing locally at the stratocumulus top. It is shown that the system develops a horizontal layered structure whose evolution is determined by molecular transport. A relatively thin inversion with a constant thickness $h = \kappa/w_e$ is formed on top and travels upwards at a mean velocity $w_e \simeq 0.1(\kappa|b_s|\chi_c^2)^{1/3}$, where $\kappa$ is the mixture-fraction diffusivity, $b_s < 0$ is the buoyancy anomaly at saturation conditions $\chi_s$ and $\chi_c$ is the cross-over mixture fraction defining the interval of buoyancy reversing mixtures. A turbulent convection layer develops below and continuously broadens into the cloud (the lower saturated fluid). This turbulent layer approaches a self-preserving state that is characterized by the convection scales constructed from a constant reference buoyancy flux $B_s = |b_s|w_e/\chi_s$. Right underneath the inversion base, a transition or buffer zone is defined based on a strong local conversion of vertical to horizontal motion that leads to a cellular pattern and sheet-like plumes, as observed in cloud measurements and reported in other free-convection problems. The fluctuating saturation surface (instantaneous cloud top) is contained inside this intermediate region. Results show that the inversion is not broken due to the turbulent convection generated by the evaporative cooling, and the upward mean entrainment velocity $w_e$ is negligibly small compared to the convection velocity scale $w^*$ of the turbulent layer and the corresponding growth rate into the cloud.

**Key words:** atmospheric flows, moist convection, turbulent mixing

## 1. Introduction

The marine stratocumulus-topped boundary layer plays a fundamental role in the planet radiative energy balance because of its contribution to the Earth's albedo, and accurate models of this archetype of moist convection are of primary importance in large-scale analyses of atmospheric flows (Stevens *et al.* 2005). The mixed-layer theory of Lilly (1968) has already identified the relevant parameters several decades ago, pointing to the entrainment rate at the top of the boundary layer as a determining quantity. Several refinements of this seminal work and different closures of that entrainment rate have been proposed ever since, but a clear and complete understanding of the physics of the boundary-layer top is still missing, which translates into an unacceptable variability of order 1 in current models (Stevens 2002).

† Present address: Max Planck Institute for Meteorology, Bundesstraße 53, 20146 Hamburg, Germany. Email address for correspondence: jpmellado@itv.rwth-aachen.de

Early field measurements (Caughey, Crease & Roach 1982) and large-eddy simulations (Deardorff 1980) have been tremendously improved over the last 30 years. Measurement resolutions of the order of centimetres have been reached in the second Dynamics and Chemistry of Marine Stratocumulus (DYCOMS-II) campaign (Stevens *et al.* 2003*b*), and these data have spawned several analyses of the entrainment mechanism at the cloud top (Stevens *et al.* 2003*a*; Faloona *et al.* 2005; Gerber *et al.* 2005; Haman *et al.* 2007; Haman 2009). At the same time, numerical simulations have achieved grid resolutions of the order of metres (Stevens *et al.* 2000; Moeng, Stevens & Sullivan 2005; Yamaguchi & Randall 2008; Kurowski, Malinowski & Grabowski 2009), complementing, in this way, experimental data more reliably. Stochastic methods such as the linear-eddy model (Krueger 1993; Wunsch 2003) have also been applied to the problem, exploring alternative explanations of the available data. All this work seems to confirm that entrainment occurs in a finite-sized region at the cloud top, the so-called entrainment interface layer, at least in a first stage. However, it is difficult to define this layer quantitatively, the proposed thicknesses fluctuate strongly and this zone exhibits very different mixing patterns. Moreover, structures below the centimetre scale have been documented, and the interaction between several small-scale phenomena – such as molecular mixing, droplet dynamics or phase transitions – and the large-scale motion remains partly obscure. This paper addresses one of these small-scale aspects: the role of evaporative cooling by isobaric mixing in the local dynamics of the cloud boundary.

In this context, evaporative cooling is a topic in itself and it is recurrently amended in the literature. At the stratocumulus top, the relatively warm and dry-air current descending from the upper troposphere meets the convection boundary layer and forms a strong inversion that limits the vertical growth of the latter. When a parcel of cool fluid from the cloud mixes with the upper subsiding layer, molecular transfer of heat tends to warm the former and, at the same time, mass diffusion promotes droplet evaporation, which tends to cool the resulting mixture. When this second mechanism dominates, the final mixture acquires a buoyancy smaller than that of the local environment and tends to sink, setting the fluid into motion. This phenomenon is known as buoyancy reversal (Siems *et al.* 1990; Wunsch 2003), which, in this case, is induced by evaporative cooling. The implications of such processes for the large-scale behaviour of the stratocumulus-topped boundary layer, like the observed cloud break-up (Deardorff 1980; Randall 1980), have been debated for a long time.

Among the different approaches adopted to investigate this problem, Siems *et al.* (1990) considered small-domain idealized two-layer models of the cloud top as a means to gain insight into some particular aspects of it. One of the relevant parameters that they introduced is the non-dimensional ratio $D = -b_s/b_1$ between the minimum buoyancy anomaly (relative to the lower layer) of the intermediate mixtures, $b_s$, and the buoyancy difference across the inversion, $b_1$. Shy & Breidenthal (1990) reported laboratory studies in a water tank using different liquid mixtures to create different buoyancy reversals at the density interface. Numerical studies by Siems *et al.* (1990) and Siems & Bretherton (1992) considered buoyancy reversal due to evaporative cooling, so that $b_s$ then corresponds to just saturation conditions. One conclusion is that buoyancy reversal alone cannot explain the stratocumulus break-up for the small values of $D$ typical of atmospheric conditions ($D \simeq 0.05$ or less). More recently, Wunsch (2003) confirmed this conclusion based on stochastic simulations, and pointed to the possible relevance of molecular diffusion in the general evolution of the system. The question, though, remains of what is really occurring at the interface in the case $0 < D \ll 1$.

We follow this strategy based on reduced-complexity systems and consider the cloud-top mixing layer as an idealized configuration designed to investigate particular questions about the local dynamics of the cloud boundary over length scales of the order of metres and under controlled conditions. It is emphasized that the purpose is neither the study of, nor the derivation of results directly applicable to, the whole stratocumulus-topped boundary layer (whose thickness is of the order of 1 km), but rather the understanding of elementary aspects of the cloud interface. We explore here one of these aspects, evaporative cooling, and the basic question we try to answer is: What happens when a layer of warm and dry air lies on top of a second layer, cool and moist, under buoyancy reversing conditions? It was soon realized that the condition $D > 0$, the non-dimensional Randall–Deardorff criterion (Deardorff 1980; Randall 1980), entails an unstable equilibrium state. The linear stability analysis by Mellado *et al.* (2009) indeed shows that, if $D > 0$, the system sustains an unstable mode with a characteristic time $\sqrt{4\pi\lambda/|b_s|}$, for a perturbation wavelength $\lambda$, in addition to interfacial gravity waves with a phase velocity $\sqrt{\lambda b_1/(4\pi)}$. However, these authors also argue that in the usual atmospheric conditions, the subsequent turbulent state that may arise inside the cloud is too weak to break the inversion and create cloud holes, in agreement with the series of works introduced in the previous paragraph; the turbulent motion is restricted to the cloud. The argument is that the time scale associated with the restoring force of the inversion and the time scale of the unstable downdraft are in a ratio equal to $\sqrt{D}$, and $D$ is a small number, i.e. the inversion returns to the equilibrium position fast compared to the time that the heavy mixture below needs to move downwards a distance $\lambda$. This conjecture based on the linear stability analysis and two-dimensional simulations is confirmed here by means of three-dimensional direct numerical simulations.

This investigation characterizes in depth, not only qualitatively but also quantitatively, by means of scaling laws, the evolution of the turbulent cloud-top mixing layer for the geophysically relevant case $0 < D \ll 1$. This paper is organized as follows. The formulation employed in the study, based on a mixture-fraction variable $\chi$, is summarized in § 2. The general evolution of the system is described in § 3 with the help of visualizations, and § 4 considers in detail the vertical layered structure observed in these visualizations. An inversion base can be defined at a height $z_i$ that separates an inversion layer on top, dominated by molecular transport, from a turbulent convection layer below, dominated by turbulent transport. The inversion layer is studied next in § 5, providing explicit expressions for its thickness $h$ and for the upward entrainment velocity $w_e$ as a function of the parameters of the problem. Then, the turbulent convection layer is investigated in § 6. This order of presentation emphasizes that (i) the inversion is not broken by the turbulent motion underneath and (ii) molecular transport at the base of the inversion controls the evolution of the system. As a consequence, we can construct a reference buoyancy flux $B_s$, and the corresponding convection scales characterize the turbulent region in the same way as in classical free convection (Deardorff 1970). Before the concluding remarks, § 7 looks at the results from three different points of view: classical turbulent convection, mixing across a density interface and the stratocumulus-topped boundary layer.

## 2. Formulation

A simplified formulation based on a mixture-fraction variable $\chi$ is used (Albrecht, Penc & Schubert 1985; Bretherton 1987). Physically, the mixture fraction is equal to

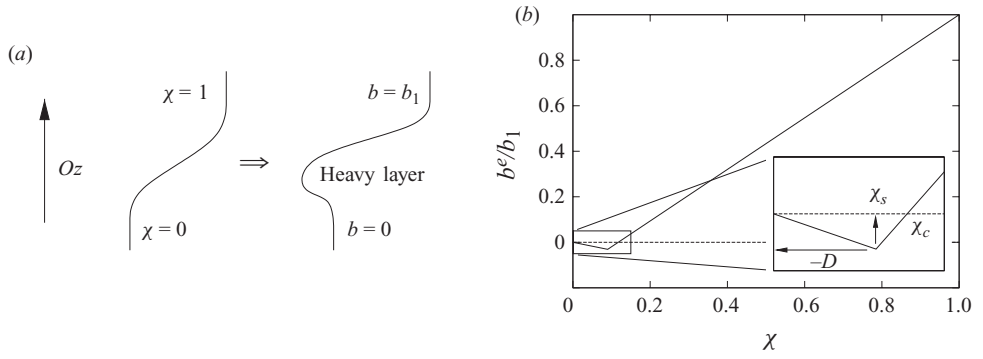


FIGURE 1. Vertical structure of the cloud top (*a*) in terms of the mixture fraction $\chi$ and the buoyancy $b$. Buoyancy mixing function $b^e(\chi)$ from (2.2) for reference case A11 in table 1; inset shows the associated parameters (*b*).

the relative amount of matter in the fluid particle that proceeds from one of two differentiated regions in the system, and it naturally appears as a normalized conserved scalar measuring conserved properties, such as the total-water content and the total enthalpy at the cloud boundary under certain conditions. Details of this methodology have been recently discussed by Mellado *et al.* (2010), who argue that the major assumptions behind this approach can be summarized as follows: (i) the liquid phase can be described as a continuum, (ii) local thermodynamic equilibrium exists and (iii) the liquid-phase diffusivity is equal to that of vapour and dry air. Estimates indicate that the conditions required for the validity of these premises are generally not met at the top of stratocumulus clouds, and therefore some caution should be exerted when drawing connections with the real atmospheric problem. The main reasons are that droplets, with a number density of the order of $1\,\mathrm{mm}^{-3}$ and a typical diameter of $10\,\mu\mathrm{m}$, are too scarce and too large for the two-fluid approximation. However, in spite of these limitations, this methodology has been very helpful in the study of some aspects of latent-heat effects at the cloud boundary, using $\chi$ as a prognostic as well as a diagnostic variable. At the same time, this formulation provides the limit of very small droplets for more sophisticated physical models of two-phase flows. On top of conditions (i)–(iii), the relatively small velocity fluctuations and the small domain size favour an incompressible framework. Last, the small variations in the density field (less than 5 %) justify the Boussinesq approximation.

The cloud-top mixing layer, by definition, consists of two infinite horizontal layers of moist air: the upper region, which is warm and unsaturated, and the lower region, which is cool and saturated (condensate-laden). The lower layer (cloud) is chosen to correspond to $\chi = 0$, and the upper layer (cloud-free) corresponds to $\chi = 1$ (see figure 1*a*). No mean shear is considered in this study, and the lapse rates inside each layer are set to zero. The frame of reference is chosen with the axis $Oz$ along the vertical and pointing upwards, and therefore perpendicular to the two horizontal layers parallel to the plane $x_1Ox_2$. The system is statistically homogeneous inside the horizontal planes, and the data inside these planes are used to construct the different statistics, which depend then on the vertical coordinate $z$ and the time $t$.

In addition to the mixture fraction $\chi(\boldsymbol{x}, t)$, the problem is described in terms of the dependent variables $\boldsymbol{v}(\boldsymbol{x}, t)$ representing the velocity vector, with components $(v_1, v_2, w)$ along the directions $Ox_1$, $Ox_2$ and $Oz$, respectively, and the buoyancy

$b(\boldsymbol{x}, t)$. The evolution in time of these fields is determined by

$$\left.\begin{aligned} \frac{\partial \boldsymbol{v}}{\partial t} + \boldsymbol{\nabla}\cdot(\boldsymbol{v}\otimes\boldsymbol{v}) &= -\boldsymbol{\nabla} p + \nu\nabla^2\boldsymbol{v} + b\boldsymbol{k}, \\ \boldsymbol{\nabla}\cdot\boldsymbol{v} &= 0, \\ \frac{\partial \chi}{\partial t} + \boldsymbol{\nabla}\cdot(\boldsymbol{v}\chi) &= \kappa\nabla^2\chi, \\ b &= b^e(\chi). \end{aligned}\right\} \tag{2.1}$$

The parameter $\nu$ is the kinematic viscosity, $\kappa$ is the scalar diffusivity, $p$ is a modified pressure divided by the reference density and $\boldsymbol{k}$ is the unit vector along $Oz$.

The buoyancy mixing function $b^e(\chi)$, describing the thermodynamics of the system, is prescribed as

$$\frac{b^e(\chi)}{b_1} = -\frac{D}{\chi_s}\chi + \left(\frac{1+D}{1-\chi_s} + \frac{D}{\chi_s}\right)\delta_s \ln\left[\exp\left(\frac{\chi-\chi_s}{\delta_s}\right) + 1\right], \tag{2.2}$$

and is depicted in figure 1(*b*). It is defined in terms of the saturation mixture fraction $\chi_s$ and the buoyancy-reversal parameter:

$$D = -\frac{b_s}{b_1}, \tag{2.3}$$

where $b_s = b^e(\chi_s)$. There is a first branch $\chi < \chi_s$ in which $b$ varies between 0 and the buoyancy $b_s$ at saturation conditions $\chi_s$ and which corresponds to the cloud. There is a second branch $\chi > \chi_s$ where the buoyancy increases up to $b_1$, the strength of the stable inversion due to the density difference between the lower and upper horizontal layers. These two branches are finally smoothed over an interval $\delta_s$ in mixture-fraction space due to smoothness requirements imposed by the numerical scheme. An important derived quantity is the cross-over mixture fraction

$$\chi_c = \frac{\chi_s + D}{1 + D}, \tag{2.4}$$

which partitions the field at each time into a negatively buoyant region $\{\boldsymbol{x} : \chi(\boldsymbol{x}) \in (0, \chi_c)\}$ and a positively buoyant region $\{\boldsymbol{x} : \chi(\boldsymbol{x}) > \chi_c\}$. The consequence of the nonlinear relation between $\chi$ and the thermodynamics, represented by $b^e(\chi)$, is that the two-layer structure in terms of the conserved quantities implies a three-layer structure in terms of the buoyancy, as shown in figure 1(*a*), which is unstable if $D > 0$.

The initial condition is specified by

$$\chi(\boldsymbol{x}, 0) = \frac{1}{2}\left[1 + \mathrm{erf}\left(\frac{z+\zeta}{2\delta}\right)\right], \tag{2.5}$$

where the vertical displacement $\zeta(x_1, x_2)$ is used to generate a broadband perturbation. The background mixture-fraction field is obtained by setting $\zeta \equiv 0$ in the equation above. The gradient thickness

$$\delta_\chi(t) = \frac{1}{(\partial\langle\chi\rangle/\partial z)_{max}} \tag{2.6}$$

is often used to measure the depth of a mixing layer, where $\langle\chi\rangle$ is the mean mixture fraction. For the unperturbed case $\zeta \equiv 0$, the relation to $\delta$ in (2.5) is $\delta_{\chi,0} \simeq 3.54\delta$. The perturbation vertical displacement $\zeta(x_1, x_2)$ is characterized by a Gaussian power spectral density centred at some given spatial frequency $1/\lambda$ and with a standard

| | $\Delta T_l$ (°C) | $\Delta q_t$ (g kg$^{-1}$) | $q_{l,c}$ (g kg$^{-1}$) | $D$ | $\chi_s$ | $\chi_c$ | $f_1$ | $f_2$ |
|---|---|---|---|---|---|---|---|---|
| A11 | 9.7 | −7.5 | 0.5 | 0.031 | 0.09 | 0.117 | 1.33 | 0.48 |
| A21 | 8.5 | −8.4 | 0.5 | 0.062 | 0.09 | 0.143 | 1.37 | 0.53 |
| A12 | 13 | −8.2 | 1.2 | 0.031 | 0.18 | 0.205 | 1.40 | 0.54 |

TABLE 1. Simulation series. Reference case A11 taken from field measurements of nocturnal marine stratocumulus (Stevens *et al.* 2003*a*): $\Delta T_l$, jump across the inversion in liquid-water static energy temperature; $\Delta q_t$, jump in total-water content; $q_{l,c}$, cloud liquid-water content. Cases A21 and A12 are derived to investigate the effects of the buoyancy-reversal parameters $D$ and $\chi_s$ independently. The cross-over mixture fraction $\chi_c$ is defined in (2.4). The last two columns contain the prefactors of the upward mean entrainment velocity (cf. (5.6)) and the rate of broadening of the convection layer (cf. (6.12)).

deviation equal to $1/(6\lambda)$, so that there is practically no energy with spatial frequencies below $1/(2\lambda)$. The phase of $\zeta$ is random.

The initial velocity field is set to zero. This implies that the mean velocity field remains zero for all times because of the horizontal statistical homogeneity, the symmetries of the problem and the solenoidal character of the velocity field.

The problem so defined depends on the parameters $\{\nu,\ \kappa,\ b_1,\ b_s,\ \chi_s\}$ and the additional set $\{\lambda,\ \zeta_{rms},\ \delta\}$ characterizing the initial condition. Dimensional analysis shows that the general solution can be expressed in non-dimensional form in terms of the non-dimensional quantities $\{Pr,\ D,\ \chi_s\}$, where the Prandtl number $Pr = \nu/\kappa$ has been introduced, and those corresponding to the initial condition. One of the contributions of this study is precisely the derivation of particular non-dimensional expressions for the evolution of quantities of physical relevance over a self-preserving regime, approximately independent of the initial conditions, which develops after an initial transient. The Prandtl number is set to 1 in all the cases, so that the parameter space we consider is $\{D,\ \chi_s\}$, in particular, the region $D \ll 1$ and $\chi_s \ll 1$, characteristic of atmospheric conditions at the top of the stratocumulus clouds (Stevens *et al.* 2005).

The set of configurations analysed in this study is defined in table 1. The reference case A11 corresponds to field measurements of nocturnal marine stratocumulus during the first research flight RF01 of the DYCOMS-II field campaign (Stevens *et al.* 2003*a*). The effects of the buoyancy-reversal parameters $D$, the strength of the reversal, and $\chi_s$, the extent of the reversal in mixture-fraction space, are considered in the derived configurations A21 and A12, respectively.

Details about the numerical algorithm can also be found in Mellado *et al.* (2010). The transport equations, written in Cartesian coordinates, are solved using finite differences on a structured mesh: sixth-order compact Padé schemes for the first- and second-order spatial derivatives and a fourth-order Runge–Kutta scheme for the time advancement. The Poisson equation is solved using Fourier decomposition along the periodic horizontal planes $x_1 O x_2$ in order to reduce it to a set of one-dimensional second-order equations, equations that are solved consistently with the high-order compact schemes used to compute the derivatives. No-penetration free-slip boundary conditions are imposed at the top and the bottom.

With respect to the specifics of the numerical simulations used in this paper, the grid size is $2048 \times 2048 \times 1536$, where the grid stretching in the vertical direction leads to a domain height of about $1.1 L_0$ if $L_0$ is the horizontal size of the computational domain. The viscosity $\nu$ is such that the reference Rayleigh number is $Ra = b_1 L_0^3/(\nu\kappa) = 4 \times 10^{11}$. The smoothing parameter in the buoyancy mixing function is $\delta_s = 0.09/16$. The initial

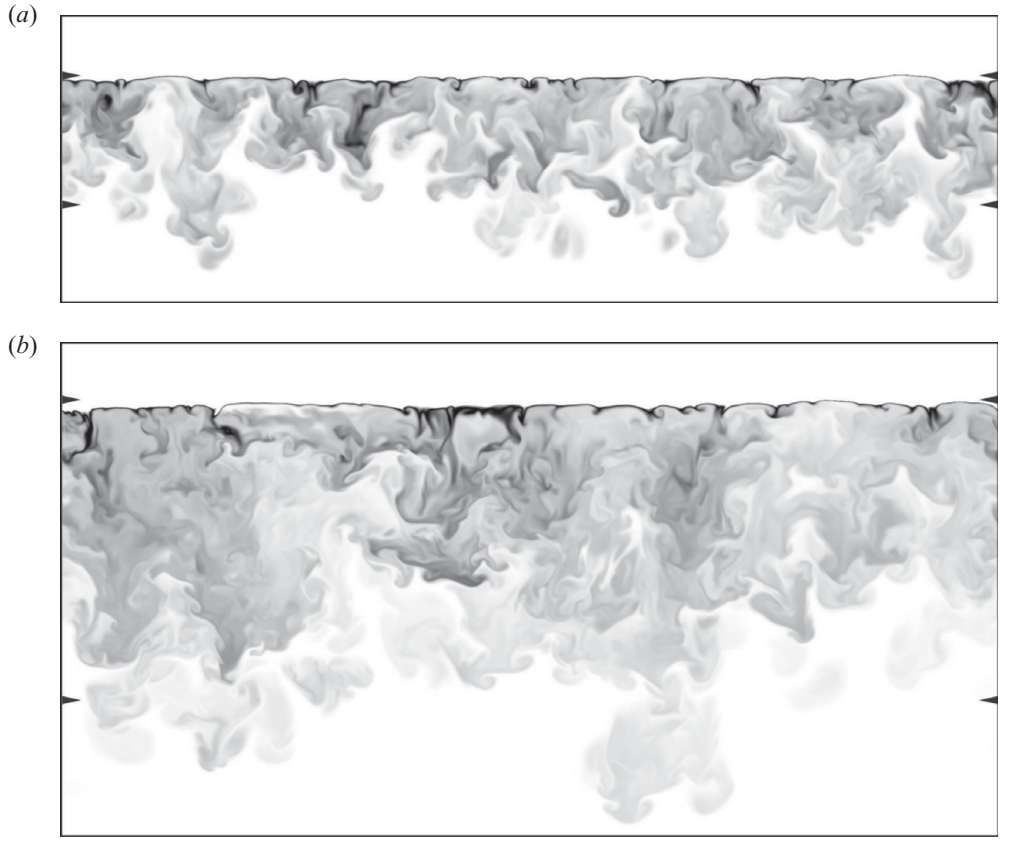


FIGURE 2. Evolution inside a vertical plane of the negative buoyancy field, with grey scale varying between black for $b = b_s$ (minimum) and white for zero: (*a*) $t_1(B_s/\delta_{\chi,0}^2)^{1/3} = 7.96$; (*b*) $t_2(B_s/\delta_{\chi,0}^2)^{1/3} = 15.4$. Upper triangular side marks indicate the position of the inversion base at $z = z_i$, and lower ones correspond to $z = z_i - z^*$.

thickness of the inversion layer is set to $\delta_{\chi,0} = 0.023L_0$, so that the corresponding thickness $\chi_c\delta_{\chi,0}$ of reversing mixtures is initially resolved by about 6 points. The initial perturbation $\zeta$ is defined by $\lambda = \delta_{\chi,0}/1.5$ and the root-mean-square (r.m.s.) is $\zeta_{rms}/\delta_{\chi,0} = 0.1$. The system is temporally evolving and the mixing region grows in time; the simulation is stopped at $t_2$ to avoid finite-domain-size effects, when the thickness of the turbulent region is about one half of the horizontal domain size (about $20\delta_{\chi,0}$) and the pressure fluctuation at the boundaries is about 2 % of the maximum inside the turbulent zone. Grid independence studies are presented in the Appendix.

## 3. Visualizations

Figure 2 presents the negative buoyancy field inside vertical planes at two different times, $t_1$ and $t_2 > t_1$, using a grey scale to indicate its magnitude: zero buoyancy in white and minimum buoyancy $b = b_s$ in black. (The vertical extent shown is only a fraction of the size of the computational domain.) Two features are worth noticing. First, a temporally evolving turbulent convection layer develops inside the cloud beneath the inversion as a consequence of the buoyancy-reversal instability. Cool-fluid downdrafts form in the cusps between the domes conforming the cloud

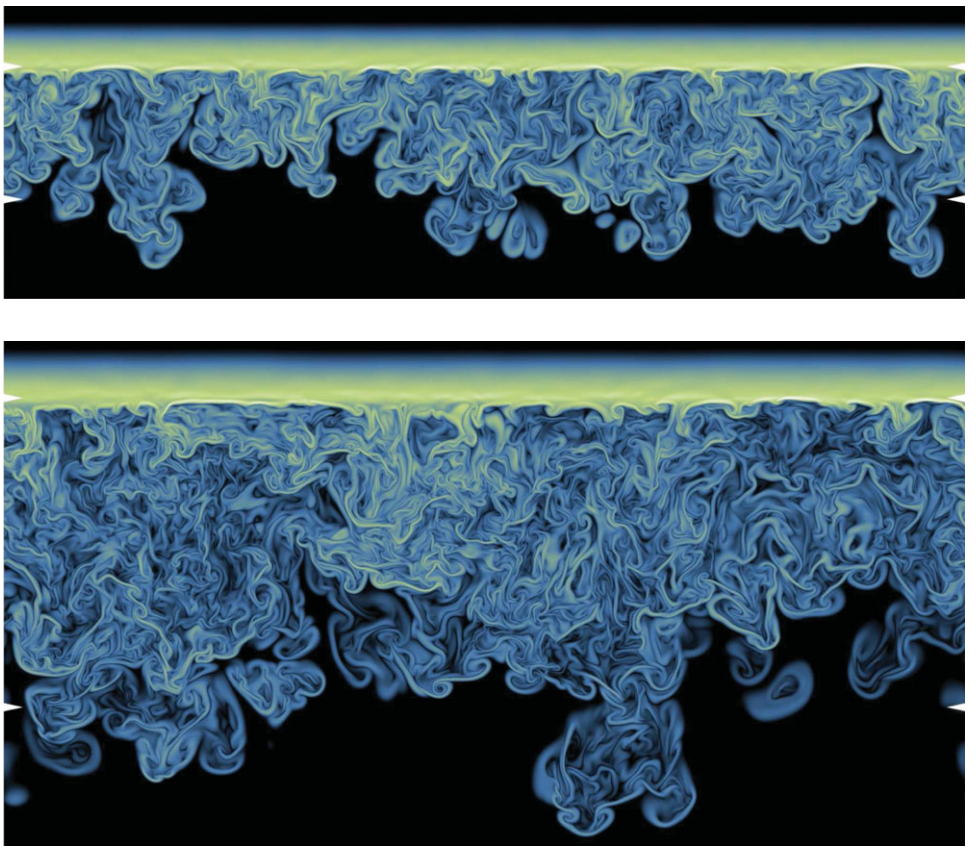


FIGURE 3. Evolution inside a vertical plane (same as figure 2) of the logarithm of the scalar dissipation rate $\epsilon_\chi$. Colour scale starting at black for the threshold $10^{-6}\max\{\langle\epsilon_\chi\rangle\}$ and increasing in the sequence blue–brown–white.

top, domes created by the corresponding upwelling motion in between. Second, the coldest (heaviest) mixtures corresponding to the iso-surface $\chi(\boldsymbol{x},t)=\chi_s$ concentrate in thin horizontal zones near the top of the cloud, whose mean vertical position is not appreciably displaced in the vertical direction between the two times $t_1$ and $t_2$. These layers containing especially cold mixtures are thickened at the base of the downdrafts because of the local straining motion, but no hole is formed through which pure fluid from above penetrates deep inside the cloud; the cloud top is not broken by the evaporatively driven motion.

This previous description is very reminiscent of thermal convection below a cold surface (Townsend 1959; Deardorff & Willis 1967; Turner 1973; Adrian, Ferreira & Boberg 1986; Siggia 1994; Ahlers, Grossmann & Lohse 2009), and this observation will be used below. The difference is, of course, that the upper boundary of the turbulent convection layer, the inversion base, is fluctuating here; more specifically, the instantaneous saturation surface $\chi(\boldsymbol{x},t)=\chi_s$ imposes the condition $b(\boldsymbol{x},t)=b_s$ on it, but the motion of this saturation surface (the instantaneous cloud top) is part of the solution.

The layered vertical structure of the system is better appreciated in figure 3 in terms of the local scalar dissipation rate $\epsilon_\chi=2\kappa|\boldsymbol{\nabla}\chi|^2$. Inside the convection layer, the

scalar field develops a lamellar structure typical of turbulent mixing, also observing the intermittent character of this region as irrotational fluid from the cloud below is entrained into the turbulent zone. In addition, this visualization shows a distinct horizontal stripe that sits on top of this convection layer, the so-called interfacial or inversion layer. The relatively strong scalar gradient found there is caused by the mean field $\langle\chi\rangle$ growing from small values $\chi < \chi_c$ inside the lower half space to the upper bound $\chi = 1$ inside the upper half space over a relatively short distance. This region is stably stratified and therefore it supports waves, which can be excited by the turbulent motion below.

Figure 4 shows the buoyancy field as in figure 2 throughout a horizontal plane close to the cloud top, in particular at the height where the horizontal velocity fluctuation is maximum. A cellular pattern is seen clearly, where the cells represent the domes below which the cloud fluid from the lower layer is ascending, their grey tones precisely indicating partially mixed conditions. Among these cells there is a more-or-less connected network of black-and-white troughs that represents the mild local penetration of the upper layer through this reference plane as the fluid is pulled down by the falling plumes underneath. The black regions inside these troughs indicate the coldest mixtures that develop in the vicinity of the saturation surface and that ultimately cause the motion. The horizontal divergence $v_{1,1} + v_{2,2}$ was also calculated, and its structure is very similar to that in figure 4 – the grey cells correspond to positively diverging regions and the meandering canyons around them are the converging zones, with a negative horizontal divergence and a corresponding positive extensional strain $w_{,z}$ in the vertical direction.

It is worth noting that these downdrafts are not isolated structures but organized into drapes reminiscent of the cracked morphology that is often observed from above the cloud deck (Nicholls 1989; Gerber *et al.* 2005; Stevens *et al.* 2005). These structures have also been documented in free convection next to a horizontal surface, where they are referred to as sheet-like plumes (Asaeda & Watanabe 1989; Goldstein & Volino 1995; Theerthan & Arakeri 2000; Flack, Saylor & Smith 2001). In agreement with the observations made in free convection, visualizations here show that these (convection) lines move randomly as the system develops in time and they are the birth place of the plummeting thermals that transport the stratifying scalar $\chi$ into the turbulent region beneath the inversion. Some of the convection cells amalgamate to create larger ones, whereas some others are sucked down by the downdrafts, the characteristic size increasing with time, as appreciated by comparison of figures 4($a$) and 4($b$). However, as already remarked before, this coherent motion does not create any hole through the density interface – there is no finger of pure upper layer fluid penetrating across the inversion deep into the lower region – because its inertia is not strong enough compared with the restoring force imposed by $b_1$. In other words, the corresponding bulk Richardson number is simply too high, as later documented in § 7.

## 4. Vertical structure of the system

Average profiles are now considered in order to be more concise about the layered structure observed before. For this purpose, the vertical distance $z$ will be measured with respect to the height $z_i(t)$ of the inversion base. This reference position is defined in terms of the maximum gradient of the mean buoyancy, one of the possible choices (Sullivan *et al.* 1998; Moeng *et al.* 2005). We will see that this location coincides with that of the maximum gradient of the mixture fraction due to the functional relation between both scalars, and any of them can be used in the calculation of $z_i$. The usual

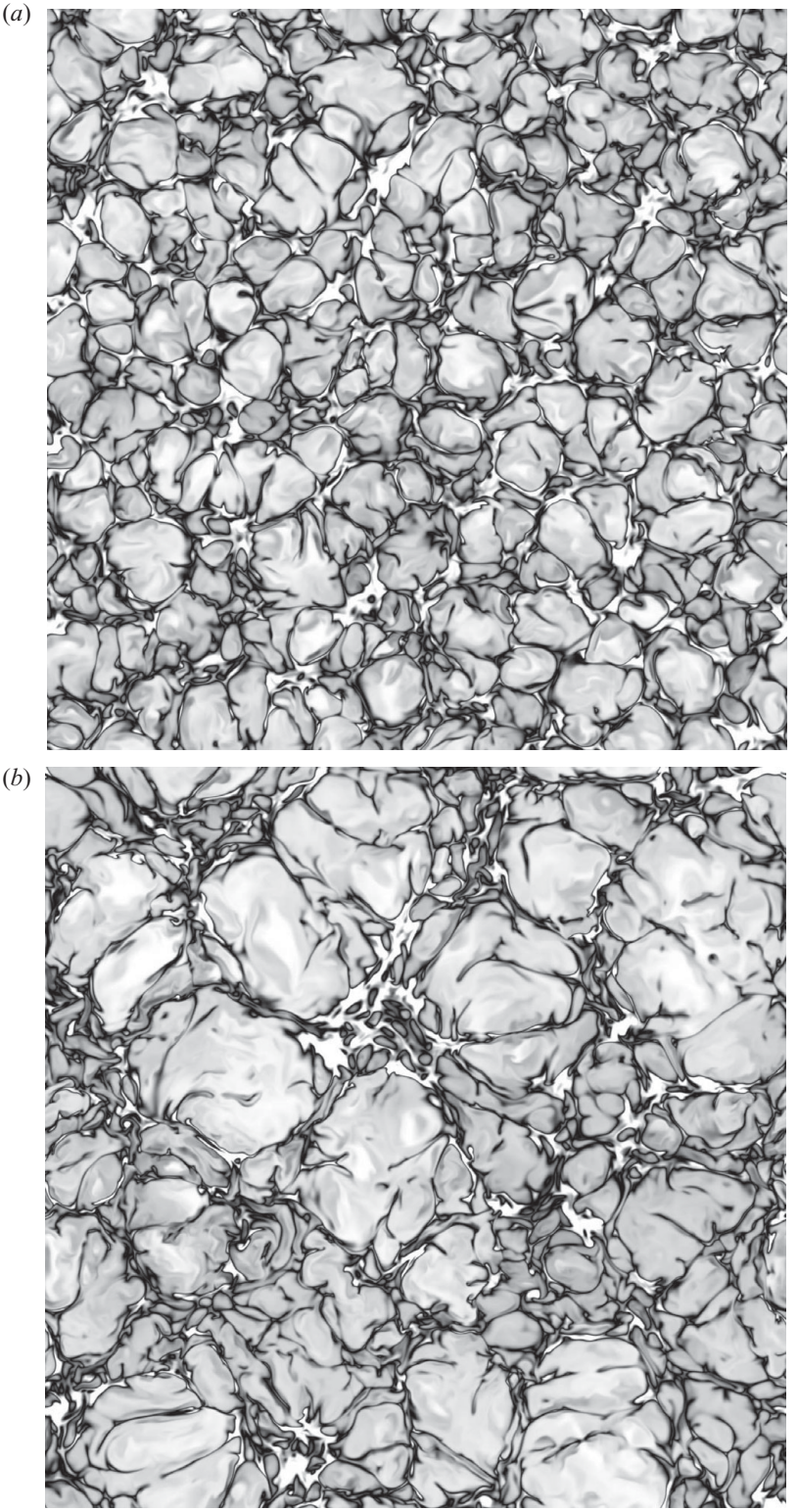


FIGURE 4. Evolution inside a horizontal plane just beneath the inversion of the negative buoyancy field. For legend see figure 2.

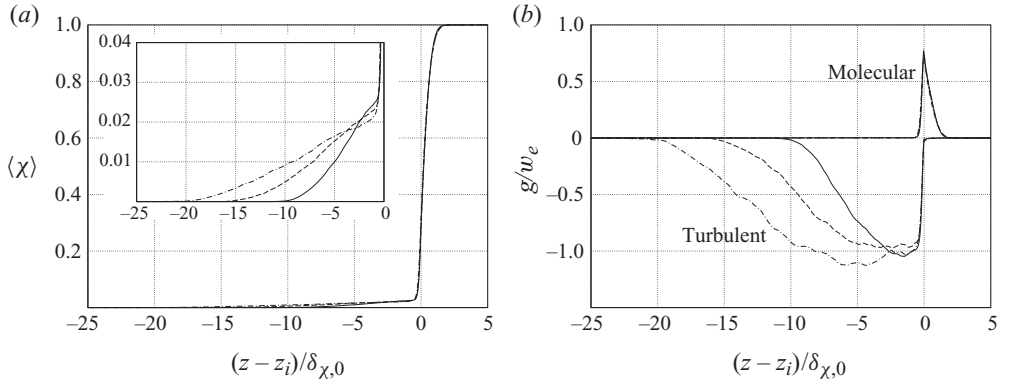


FIGURE 5. Profiles of mean mixture fraction ($a$) at different times: solid line, $t_1(B_s/\delta^2_{\chi,0})^{1/3} = 7.96$; dashed line, $t(B_s/\delta^2_{\chi,0})^{1/3} = 12.0$; dot-dashed line, $t_2(B_s/\delta^2_{\chi,0})^{1/3} = 15.4$. Budget of the transport equation ($b$) at the same times: turbulent flux, $g = \langle w'\chi'\rangle$; (negative) molecular flux, $g = \kappa\partial\langle\chi\rangle/\partial z$.

justification for this particular definition of the inversion base is that it corresponds to the height of maximum mean stratification $N^2 = \partial\langle b\rangle/\partial z$ and therefore the vertical motion is inhibited the strongest at this height. Results will confirm that this definition is indeed an appropriate one.

The average mixture fraction $\langle\chi\rangle$ is presented in figure 5($a$) at equidistant times between $t_1$ and $t_2$ for the reference case A11. These curves are mainly characterized by the relatively thin inversion region around $z_i(t)$ over which the variations in $\langle\chi\rangle$ are of order 1, and by the fact that the shape of this inversion does not change significantly during that interval of time. On the other hand, the variation of the mixture fraction in the convection layer for $z < z_i$ is notoriously smaller; only a fraction of the saturation value $\chi_s$ (equal to 0.09 for this reference case), and the zoomed view in the inset of the figure is really needed to appreciate the details of this turbulent zone. A second difference as compared to the inversion is that $\langle\chi\rangle$ within the convection layer does vary in time, broadening downwards by about a factor of 2 between $t_1$ and $t_2$ and decreasing slightly in magnitude.

The mean fluxes on the right-hand side of the transport equation of $\langle\chi\rangle$,

$$\frac{\partial\langle\chi\rangle}{\partial t} = \frac{\partial}{\partial z}\left(\kappa\frac{\partial\langle\chi\rangle}{\partial z} - \langle w'\chi'\rangle\right), \tag{4.1}$$

plotted in figure 5($b$), clarify the layered structure of the system even further. (Henceforth, an apostrophe indicates a fluctuating field.) This figure shows that the inversion base $z_i(t)$ unambiguously separates the upper region dominated by molecular transport, the inversion, from the lower region within the cloud dominated by turbulent transport, the convection layer. In between, a relatively thin transition region can be identified over which the turbulent flux falls to a very small value in favour of a dominant molecular flux.

The saturation surface $\chi(\boldsymbol{x}, t) = \chi_s$ (instantaneous cloud top) remains within that transition layer, very near to the inversion base. Figure 6 presents the probability density function (p.d.f.) of the vertical distance between the saturation surface and the inversion base at $z_i$. It is seen that excursions of the iso-surface into the region $z > z_i$ are rare, and the mean position stays very close to the base of the inversion, as indicated by the range of abscissas spanned in figure 6. It is true that this mean

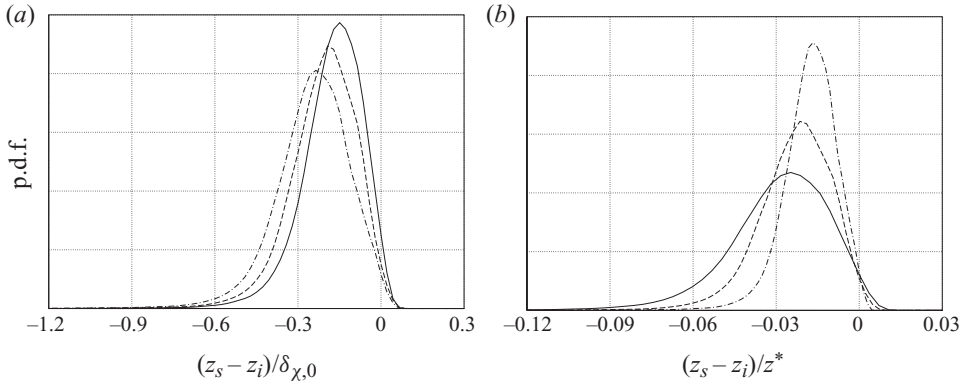


FIGURE 6. Probability density function of the vertical distance between the instantaneous cloud top at $z = z_s(x, y)$ and the inversion base at $z = z_i$, normalized by the initial gradient thickness $\delta_{\chi,0}$ in $(a)$ and by the characteristic depth of the convection layer $z^*$ in $(b)$, at different times. For legend see figure 5.

position of the fluctuating surface mildly moves downwards in time and the standard deviation increases slightly, but at a rate much slower than the thickening of the convection layer observed before in figure 5. This last remark is clearly exposed by figure 6$(b)$, where the random variable is normalized with $z^*(t)$, a length scale representing the thickness of the convection layer. (This convection scale will be discussed in detail in § 6.) In fact, this p.d.f. allows us to be more precise about the previous statement in § 3: 'no hole is formed at the cloud top through which a finger of pure fluid from the upper layer penetrates deep into the cloud layer'; it means that the vertical position of the instantaneous cloud top remains next to the inversion base within a distance that is much smaller than, and that does not scale with, the thickness $z^*$ of the turbulent convection layer. (Actually, its position tends to a delta function at $z_i(t)$ in these relative terms.)

This behaviour of the saturation surface is important to understand the relations between the statistics of the mixture fraction $\chi$ and those of the buoyancy $b$. Both scalars are related by the nonlinear mixing function $b^e(\chi)$ depicted in figure 1$(b)$. However, the nonlinearity is set by the discontinuity in the derivative at $\chi = \chi_s$, and we have learnt in the previous paragraph that this iso-surface remains right underneath the inversion base. Therefore, the mixture fraction and the buoyancy are linearly related inside the inversion layer. In particular, the gradient thickness,

$$\delta_b = \frac{b_1}{(\partial \langle b \rangle / \partial z)_{max}}, \tag{4.2}$$

is approximately equal to $\delta_\chi(1 - \chi_s)/(1 + D)$, and the inversion base, defined in terms of the maximum of the mean buoyancy gradient, can also be calculated based on the maximum gradient of the mean mixture fraction, as anticipated in the first paragraph of this section. In the same way, the linear relation $b = -(D/\chi_s)\chi$ holds pointwise in almost all of the convection layer. The complete variation of the mean buoyancy is shown in figure 7$(a)$: the inversion profile follows that of the mixture fraction in figure 5$(a)$, and the variation inside the convection region mimics that of $\langle \chi \rangle$ but simply with an opposite sign. The essential departure between the mixture-fraction and the buoyancy fields ($\chi$ is a conserved scalar whereas $b$ is not) is restricted to a transition layer adjacent to the inversion base at $z = z_i$.

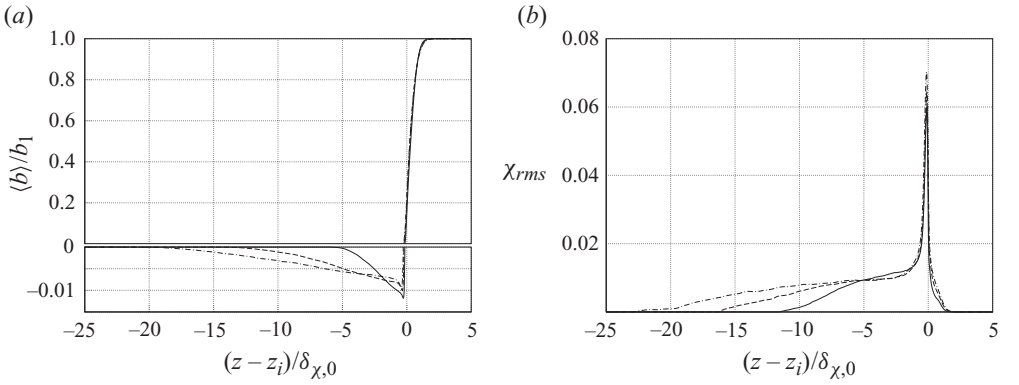


FIGURE 7. Profiles of mean buoyancy (*a*) at different times (note that a different scale is used for $\langle b\rangle < 0$). Profiles of mixture-fraction fluctuation intensity (*b*) at different times. For legend see figure 5.

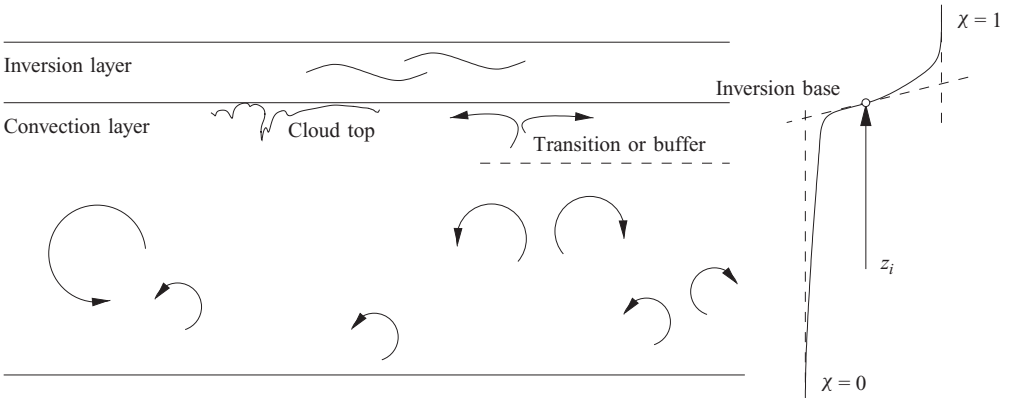


FIGURE 8. Sketch representing the layered structure of the system: inversion layer on top, dominated by molecular transport and supporting waves; convection layer below, dominated by turbulent transport and containing a transition layer just beneath the inversion base at $z = z_i(t)$.

In terms of the scalar turbulent fluctuation with respect to the mean profiles discussed so far, figure 7(*b*) plots the mixture-fraction r.m.s. and shows that this fluctuation is very intense in relative terms inside the convection layer because its magnitude is comparable to the mean values presented in figure 5(*a*). There is also a dominant peak in the profile close to $z = z_i$, which simply quantifies the oscillatory motion of the strong gradient region illustrated in the visualizations of § 3. Above this point, the fluctuation decays rapidly across the inversion, though it is non-zero, indicating inhomogeneities and therefore some motion inside it. However, it is reminded that the vertical transport due to this motion is small compared to the molecular contribution, as observed in figure 5(*b*).

As a summary of this section, figure 8 sketches the vertical structure of the cloud-top mixing layer. The inversion base at $z = z_i(t)$, defined in terms of the maximum mean buoyancy gradient, partitions the space into two very differentiated regions: the inversion layer on top, dominated by molecular processes, and the convection layer below, dominated by turbulent transport. In the following sections, we investigate

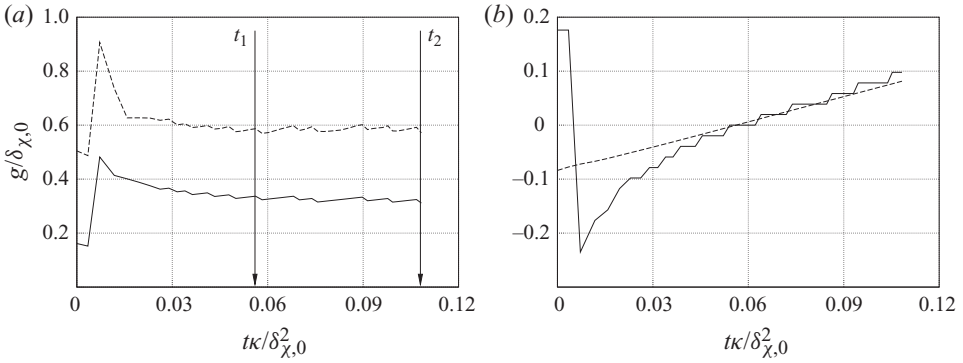


FIGURE 9. Temporal evolution of inversion properties ($a$): solid line, area $g = \int (1 - \langle\chi\rangle)\,\mathrm{d}z$ as used in (5.1); dashed line, thickness $g = h$ as defined by (5.4). Temporal evolution of the height of the inversion base ($b$): solid line, $g = z_i - z_i(t_1)$ as obtained from the definition in terms of $\langle\chi\rangle$; dashed line, $g = \int_{t_1} w_e \mathrm{d}t'$ using (5.3).

each of them separately; first, we consider the details of the inversion layer, in § 5, which is intricately related to the upward mean entrainment velocity, and then we look at the turbulent convection layer, in § 6, where a self-preserving state is observed.

## 5. The inversion layer

Let us now examine the inversion layer more closely. Integration of the transport equation (4.1) for $\langle\chi\rangle$ from $z_i(t)$ upwards leads to

$$\frac{\mathrm{d}}{\mathrm{d}t}\left[\int_{z_i}^{\infty}(1-\langle\chi\rangle)\,\mathrm{d}z\right] = \frac{\kappa}{\delta_\chi} - \langle w'\chi'\rangle(z_i,t) - (1-\chi_i)\frac{\mathrm{d}z_i}{\mathrm{d}t}, \tag{5.1}$$

where $\chi_i(t) = \langle\chi\rangle(z_i(t),t)$ is the mean mixture fraction at the inversion base . According to this equation, the evolution of the area enclosed by the profile $\langle\chi\rangle$ and the reference value $\chi = 1$ within the inversion is proportional to the difference between the mean fluxes at the inversion base and its vertical displacement measured in terms of the (upward) mean entrainment velocity:

$$w_e = \frac{\mathrm{d}z_i}{\mathrm{d}t}. \tag{5.2}$$

Figure 9($a$) shows that this area remains approximately constant, as already anticipated by inspection in figure 5($a$), which suggests that the terms on the right-hand side of (5.1) approximately balance each other. Furthermore, figure 5($a$) also shows that $\langle w'\chi'\rangle(z_i,t) \ll \kappa/\delta_\chi$, i.e. the turbulent flux at the inversion base is negligible compared with the molecular flux, and therefore the dominant balance in (5.1) occurs between this molecular transport and the displacement velocity $w_e$. Hence, $w_e$ can be computed from local properties of the mean mixture-fraction profile at the inversion base at time $t$ according to

$$w_e \simeq \frac{\kappa}{h}, \tag{5.3}$$

where the thickness of the inversion $h$ is defined in terms of the mean gradient at $z_i$ as

$$h = \delta_\chi(1-\chi_i). \tag{5.4}$$

The degree of accuracy with which this dominant balance between $w_e = \mathrm{d}z_i/\mathrm{d}t$ and $\kappa/[\delta_\chi(1-\chi_i)]$ in (5.1) is achieved is illustrated in figure 9(*b*), which plots $z_i(t)$ as obtained from the identification of the maximum gradient in the mean mixture-fraction profile at each time $t$ and the quantity $z_i(t_1)+\int_{t_1} w_e \mathrm{d}t$, where $w_e$ is calculated according to (5.3). The approximate collapse beyond $t_1$ confirms the hypothesis, which is satisfied with a relative error of about 16 % (relative difference of the slopes of the curves in figure 9(*b*) between $t_1$ and $t_2$).

Figure 9(*a*) shows the thickness $h$ as a function of time for the reference case A11. The most important property of this curve is that it approaches a constant value after an initial transient. Once the dependence on time $t$ drops out, dimensional analysis implies that $h \sim (\kappa^2/b)^{1/3}$, where the constant of proportionality is a function of $D$ and $\chi_s$, and $b$ is a buoyancy parameter, either $b_s$ or $b_1$. However, the steadiness of $h$ suggests a dynamic balance among the diffusion, viscosity and buoyancy, and a more specific scaling can be obtained following the classical theory of turbulent convection (Turner 1973), as discussed shortly, the only difference being that in the cloud-top mixing layer, there exists a stable inversion next to the unstable reversing region.

Let $l$ be the thickness of an inversion layer over which the stratifying agent $\chi$ varies between 0 and 1. This inversion is stably stratified, except for a zone of order $\chi_c l$ on the lower edge where the buoyancy reversal develops according to figure 1. Without molecular processes, this configuration is unstable and, if perturbed, the buoyancy-reversal instability develops (Mellado *et al.* 2009). However, when the diffusivity $\kappa$ is retained in the analysis, the inversion thickens at a rate $\kappa/l$ and may inhibit the previous instability. Since $\chi_c$ is small for the relevant atmospheric conditions, the time scale needed for the thickening of the inversion layer to cover the distance $\chi_c l$ is simply $t_d = \chi_c l^2/\kappa$. At the same time, the perturbation suffers an acceleration of order $|b_s|$ and, once it moves, it is opposed by a drag proportional to the viscosity $\nu$ and the velocity; the time needed by a perturbation of order $\chi_c l$ to cover a distance of the order $\chi_c l$ because of this mechanism is $t_b = \nu/(\chi_c l|b_s|)$. If $t_d \ll t_b$, for instance, because $l$ is small enough, then the initial perturbation is smoothed out. On the contrary, if $t_b \ll t_d$, then the buoyancy reversing regions of fluid can escape the diffusion front advancing from above, setting the fluid into motion.

This comparison of scales suggests that, in a dynamic equilibrium, the inversion is characterized by the thickness $l$ at which both times are similar, which leads to $t_d/t_b = \chi_c^2|b_s|l^3/(\kappa\nu) \sim 1$, a typical criterion based on a critical Rayleigh number. If the layer were thicker, then the reversing mixture below would fall off the inversion, thus reducing $l$; if the layer were thinner, then diffusion would increase $l$. However, free-convection studies show that critical Rayleigh numbers are normally of order $10^3$, and estimates are more accurate if the condition $\chi_c^2|b_s|l^3/(\kappa\nu) \sim 10^3$ is employed (Siggia 1994). Consequently, the thickness of the inversion is characterized by $l \sim 10[\kappa\nu/(|b_s|\chi_c^2)]^{1/3}$, suggesting the scalings

$$h = \frac{10}{f_1 \chi_c^{2/3}} Pr^{1/3} (\kappa^2/|b_s|)^{1/3}, \tag{5.5}$$

for the thickness $h$ defined in (5.4), and

$$w_e = \frac{f_1 \chi_c^{2/3}}{10} Pr^{-1/3} (\kappa|b_s|)^{1/3}, \tag{5.6}$$

for the velocity $w_e$ defined in (5.3). We, of course, recover the relations $h \sim (\kappa^2/b)^{1/3}$ and $w_e \sim (\kappa b)^{1/3}$, which were anticipated before based only on dimensional analysis; the expectation from the reasoning of the earlier paragraphs is that we obtain

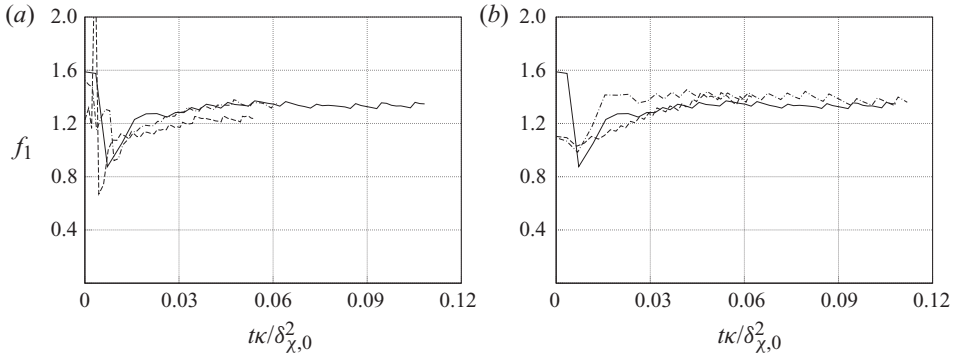


FIGURE 10. Temporal evolution of the mean upward entrainment velocity $w_e$ normalized with inversion scales as in (5.6). Effect of molecular diffusivity ($a$): solid line, reference case A11 with $\kappa_0$; dashed line, $\kappa = 2\kappa_0$; dot-dashed line, $\kappa = 4\kappa_0$. Effect of buoyancy parameters ($b$) in table 1: solid line, reference case A11; dashed line, case A21 with double $D$; dot-dashed line, case A12 with double $\chi_s$.

the leading-order dependence on $D$ and $\chi_s$, and $f_1 = f_1(Pr,\, D,\, \chi_s)$, of order 1, then represents higher-order corrections. Only the case $Pr = 1$ is considered in this study.

The scaling with respect to $\kappa$ is confirmed by figure 10($a$), which includes, in addition to the reference case A11, the curves from two additional simulations: a first one with twice and a second one with four times the diffusivity $\kappa$ of case A11. It is seen that all of the curves approach the same value, in spite of having different initial conditions and actually different computational meshes, since the last two simulations were performed on a grid with half the size of the reference mesh. Hence, the dominant role of the scalar molecular diffusivity $\kappa$ in the evolution of the system is unequivocally stated in these results, confirming the hypothesis already put forward by Wunsch (2003).

The particular functional dependence of $w_e$ on $D$ and $\chi_s$ expressed by (5.6) is more delicate because it hinges on the mechanistic argumentation presented in the previous paragraphs. Support for this scaling is given in figure 10($b$), which plots the non-dimensional function $f_1$ for the cases A11, A21 and A12 presented in table 1, covering the range of variation in the buoyancy-reversal parameters $D$ and $\chi_s$, corresponding to the typical atmospheric conditions at the stratocumulus top. Normalized velocities are indeed of order 1, and the approximately constant values observed during the last part of the simulations are collected in table 1, with $f_1$ varying between 1.33 and 1.40. The second observation is precisely that this variation among the different cases is relatively small, about 5 %, which implies that the function $f_1(D, \chi_s)$ is approximately constant in the cases of interest. This means that $w_e$ depends solely on $b_s$ to the leading order; the inversion strength $b_1$ enters only as a correction through the term $\chi_c = (\chi_s + D)/(1 + D) \simeq \chi_s(1 + D/\chi_s)$ due to the small values of $D$.

This section can be summarized as follows: the inversion base $z_i$, and therefore the inversion as a whole (see sketch in figure 8), moves upwards linearly in time with a constant thickness, and it is characterized by the inner scales constructed from $w_e$, given by (5.6), and the molecular diffusivity $\kappa$ of the stratifying scalar $\chi$ (equal to the normalized enthalpy and total water specific humidity). In particular, the thickness $h = \kappa/w_e$ is given by (5.5).

## 6. The convection layer

We now turn to the convection layer, the turbulent zone that develops below the inversion base. Integration of (4.1) from $z_i(t)$ downwards leads to

$$\frac{\mathrm{d}}{\mathrm{d}t}\int_{-\infty}^{z_i}\langle\chi\rangle\mathrm{d}z = \frac{\kappa}{\delta_\chi} - \langle w'\chi'\rangle(z_i,t) + \chi_i w_e \simeq w_e, \tag{6.1}$$

where the last step follows from $\langle w'\chi'\rangle(z_i,t) \ll \kappa/\delta_\chi$, (5.3) and (5.4), as explained in the previous section. This result is the reason for the scaling of the mixture-fraction fluxes in figure 5(*b*) in terms of $w_e$, which then yields normalized values of order 1 in the figure, in particular the normalized turbulent flux $\langle w'\chi'\rangle/w_e$ inside the turbulent convection layer. At the same time, we have learnt in the previous section that the linear relation $b = -(b_s/\chi_s)\chi$, corresponding to the left branch of the buoyancy mixing function $b^e(\chi)$, holds over most of the convection layer, outside a thin region next to the inversion base $z_i$ where the saturation surface $\chi(\boldsymbol{x},t) = \chi_s$ stays. These two facts imply that the turbulent buoyancy flux $B = \langle w'b'\rangle$ is characterized by the reference buoyancy flux

$$B_s = w_e|b_s|/\chi_s = \left(0.1 f_1 \chi_c^{2/3}/\chi_s\right) Pr^{-1/3}\left(\kappa b_s^4\right)^{1/3}, \tag{6.2}$$

where (5.6) has been used to express $w_e$ in terms of the parameters of the problem. We explore in this section several consequences of this important finding.

### 6.1. *Convection scales*

The argumentation of the previous paragraph implies that the motion inside the turbulent convection layer is determined by the molecular buoyancy flux at its upper boundary, the inversion base. This observation, in conjunction with the previous result that the cloud top concentrates in a relatively thin region next to $z_i$ and is not broken, confirms the similarity of this problem with free convection below a cold plate. Therefore, following Deardorff (1970), a convection velocity can be defined as

$$w^* = \left(z^* B_s\right)^{1/3}. \tag{6.3}$$

In the case of the cloud-top mixing layer considered in this study, a length scale $z^*$ measuring the depth of the turbulent zone is not imposed externally – the system is temporally evolving and the mixing region broadens continuously in time. One possible definition of a thickness is

$$z^* = \int B\,\mathrm{d}z/B_s, \tag{6.4}$$

based on the depth-integrated value of the turbulent buoyancy flux $B$. (If the limits of integration are not shown explicitly, the integral extends over the whole domain.) This choice is not arbitrary, but follows Deardorff (1980) in the sense that then $w^{*3} = \int B\,\mathrm{d}z$, a definition of the convection velocity $w^*$ also considered by other authors (Sayler & Breidenthal 1998; Faloona *et al.* 2005) except for a numerical factor of order unity.

Hence, the outer scales $w^*$ and

$$b^* = w^{*2}/z^* = B_s/w^*, \tag{6.5}$$

defined from $B_s$ and $z^*$ (in contrast to the inner scales derived from $w_e$ and $\kappa$), provide the magnitude of large-scale statistics within the convection layer beneath the inversion, and the corresponding profiles can be expressed as a function of only the

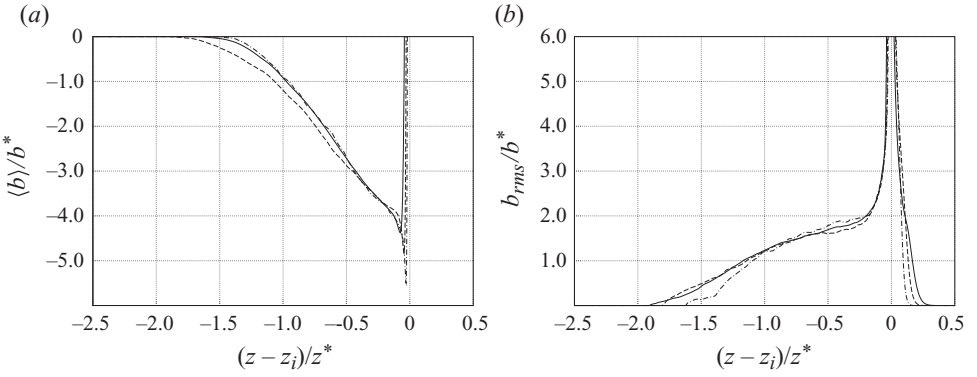


FIGURE 11. Self-similar vertical profiles of the mean buoyancy ($a$) and the buoyancy fluctuation intensity ($b$) for different times. For legend see figure 5.

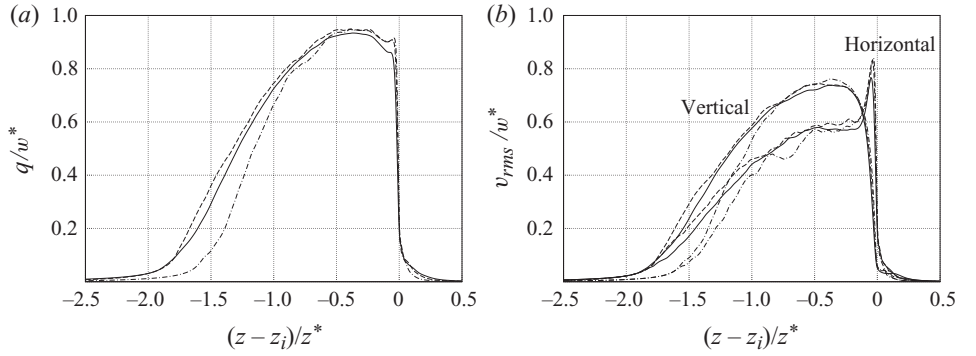


FIGURE 12. Self-similar vertical profiles of total velocity r.m.s. ($a$) and its partition into the horizontal fluctuation intensity $u_{rms} = \sqrt{R_{uu}}$ and the vertical one $w_{rms} = \sqrt{R_{ww}}$ ($b$) for different times. For legend see figure 5.

following self-similar variable:

$$\xi = \frac{z - z_i}{z^*}. \tag{6.6}$$

This is exposed, for instance, in figure 11($a$), where the curves depicting $\langle b\rangle$ at different times approximately collapse on top of each other when scaled by the convection variables, in contrast to figure 7($a$). The same is illustrated in figure 11($b$) in terms of the buoyancy fluctuation, where it is further seen that $b^*$ represents the typical r.m.s. value around the centre of the turbulent region and that the depth of the convection layer is about $2z^*$.

This characterization in terms of the convection scales within the turbulent region is very well portrayed by the statistics related to the velocity field, as observed in figure 12. Figure 12($a$) contains the turbulent kinetic energy per unit mass, $q^2/2 = (R_{ww} + R_{uu})/2$, where the vertical Reynolds stress is $R_{ww} = \langle w'w'\rangle$ and the horizontal Reynolds stress is $R_{uu} = \langle u'u'\rangle = R_{11} + R_{22} = \langle v_1'v_1'\rangle + \langle v_2'v_2'\rangle$. This figure also shows that the kinetic energy concentrates within the cloud and it is strongly capped by the inversion at $z \simeq z_i$, with a mild motion in the inversion layer, which is consistent with the fluctuation of the mixture fraction found in figure 7($b$) as well.

The partition of $q^2$ into the vertical and the horizontal energy mode is presented in figure 12($b$). Apart from the scaling in terms of $w^*$ and $z^*$, the main feature is

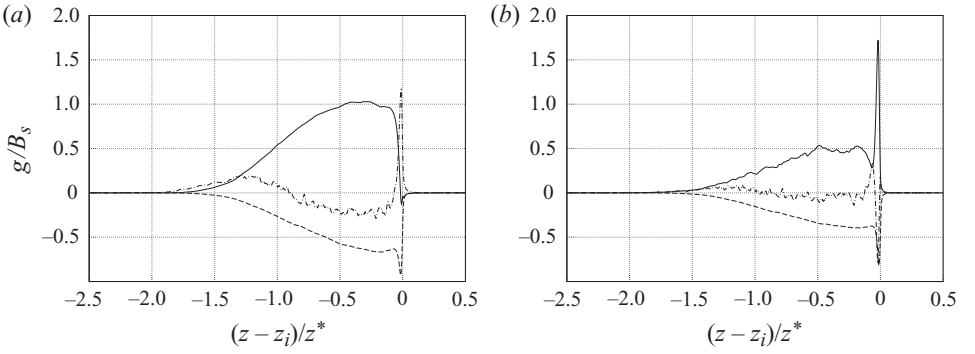


FIGURE 13. Self-similar vertical profiles of the terms in the transport equation for $q^2/2$, from (6.7), in (*a*): solid line, buoyancy production rate $g = B$; dashed line, turbulent dissipation rate $g = -\varepsilon$; dot-dashed line, turbulent transport rate $g = -\partial T/\partial z$. Same for $R_{uu}/2$, from (6.8), in (*b*): solid line, pressure–strain correlation $g = \Pi_{uu}$; dashed line, $g = -\varepsilon_{uu}$; dot-dashed line, $g = -\partial T_{uu}/\partial z$.

the anisotropy of the flow, not only because in the bulk of the convection layer, the vertical fluctuation is about 1.4 times larger than the horizontal, but also because close to the inversion base, this behaviour is reversed and the horizontal motion is much stronger than the vertical one. In fact, the maximum $u_{rms}$ in the whole convection layer occurs there, a maximum that seems to scale with $w^*$ and that forms across a distance of the order of $0.1z^*$; we will refer to this region as the transition or buffer zone.

### 6.2. *Kinetic-energy budgets*

Further insight into the vertical structure of the system sketched in figure 8, and in particular about the buffer layer, is provided by the transport equations of the velocity fluctuations. The turbulent kinetic energy evolves according to

$$\frac{\partial q^2/2}{\partial t} = -\frac{\partial T}{\partial z} + B - \varepsilon, \tag{6.7}$$

where $T = \langle w' v_i' v_i'/2 + p' w' - v_i' \tau_{iz}' \rangle$ is the turbulent flux along the vertical direction and the mean turbulent dissipation rate is $\varepsilon = \langle v_{i,j}' \tau_{ij}' \rangle$, with the viscous stress tensor being $\tau_{ij} = \nu(v_{i,j} + v_{j,i})$. The terms on the right-hand side are plotted in figure 13(*a*), having averaged the self-similar profiles $g(\xi)$ over the three times between $t_1$ and $t_2$ in order to improve statistical convergence and the clarity of the figure. The turbulent buoyancy flux $B$, being positive over most of the space, is responsible for the production of kinetic energy. This production is ultimately caused by the sheet-like plumes and thermals dropping from the instantaneous cloud top (see figure 2), which strongly correlates the heavy parcels (with negative buoyancy) with the negative vertical velocity and which sets up an upwelling motion of lighter fluid in between. A local negative value of turbulent buoyancy flux is observed around $z \simeq z_i$, but it extends over a very narrow region and it is small compared to the other two contributions on the right-hand side of the previous transport equation. The turbulent diffusion vertically redistributes the turbulent kinetic energy, transporting it from the interval $-0.7 < \xi < -0.1$, where the production is maximum towards the lower and upper edges of the turbulent zone, promoting, in this way, the broadening of the mixing region. Finally, as a consequence of the velocity fluctuations, viscous dissipation removes kinetic energy at a rate $\varepsilon$ throughout the whole convection layer although

the maximum arises in the transition zone, consistent with the sharp variation of velocity fluctuations that occurs there.

The transfer of kinetic energy between the vertical and the horizontal velocity component is quantified by the pressure–strain correlation $\Pi_{uu} = \langle p'(v'_{1,1} + v'_{2,2})\rangle$, a source term in the equation

$$\frac{\partial R_{uu}/2}{\partial t} = -\frac{\partial T_{uu}}{\partial z} + \Pi_{uu} - \varepsilon_{uu}, \tag{6.8}$$

where $T_{uu} = \langle (v'_1 v'_1 + v'_2 v'_2)w'/2 - v'_1 \tau'_{xz} - v'_2 \tau'_{yz}\rangle$ and $\varepsilon_{uu} = \langle v'_{1,j}\tau'_{xj} + v'_{2,j}\tau'_{yj}\rangle$. Figure 13($b$) shows that $\Pi_{uu}$ is positive over the whole convection layer, as expected, with a magnitude about $0.5B_s$, half of that of the turbulent buoyancy flux $B$ in figure 13($a$). The former figure also provides a measure of the intensification of this transfer process inside the transition layer, between $z_i - 0.1z^*$ and $z_i$, where the peak achieves three times larger values. This strong generation of horizontal kinetic energy determines the local behaviour of the other two terms in the transport equation for $R_{uu}$. First, the transport term is negative and indicates a transfer in physical space of $R_{uu}$ out of the buffer zone. This means that $T_{vv}$, the vertical counterpart, is about $2B_s$ inside that region in order to yield the values of $T = T_{vv} + T_{uu}$ observed in figure 13($a$), i.e. $T_{vv}$ is comparable to $\Pi_{uu}$ in that zone. Second, the dissipation rate $\varepsilon_{uu}$ develops a marked maximum in the transition zone due to the high values of $R_{uu}$. This maximum accounts for almost all of the peak in the total term $\varepsilon$ observed in figure 13($a$).

The behaviour of these energy budgets is qualitatively very similar to that observed by Leighton, Smith & Handler (2003) in evaporative cooling beneath the free surface of a water–air system, in spite of the differences in the boundary conditions (they use a rigid free-slip wall) and the fact that they force a steady regime. Both configurations, the cloud top and the water free surface, share the feature that the vertical motion is strongly hindered at some height, and this causes the negative correlation between the local vertical variation of the vertical velocity $w_{,z}$ and the local pressure high, which brings about the formation of a strong peak in the profile of $\Pi_{uu}$ beneath the inversion base, in our study, and beneath the free surface, in their work. The transport terms are also similar in both cases: $-\partial T_{uu}/\partial z$ becomes negative next to the capping interface and $-\partial T/\partial z$ strongly positive, and the major contribution to the latter arises again because of the contribution from the pressure fluctuations to the turbulent transport (not explicitly shown in figure 13($a$) for clarity). The same behaviour with respect to the total transport term $T$ has also been documented in the case of a solid no-slip boundary (Moeng & Rotunno 1990; Kerr 2001; Kunnen, Geurts & Clercx 2009).

In contrast, the dissipation profiles depend on having a slip or a no-slip boundary condition. These profiles are qualitatively similar between the cloud top and the water free surface, but, in the case of a solid wall, the dissipation develops a stronger maximum at the wall, which seems reasonable due to the no-slip constraint. One-to-one comparisons between slip and no-slip boundary conditions would be interesting in this matter to make a more quantitative statement.

### 6.3. *Explicit expressions of the growth rate*

We conclude the analysis of the convection layer with the investigation of the growth rates of the turbulent mixing region. By integrating (6.7) in space, we obtain the relation

$$\frac{\mathrm{d}}{\mathrm{d}t}(c_q z^* w^{*2}) = 2(1 - c_\varepsilon)w^{*3}, \tag{6.9}$$

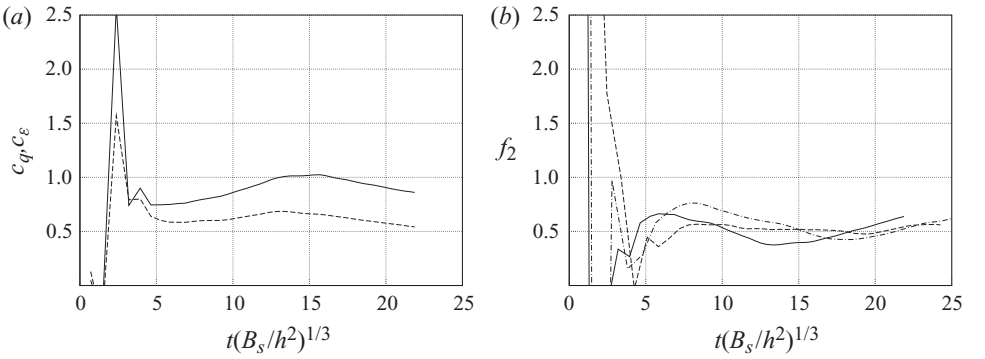


FIGURE 14. Integrated turbulent quantities for case A11 normalized by the convection scales, in (*a*): solid line, kinetic energy $c_q$; dashed line, dissipation rate $c_\varepsilon$. Temporal evolution of the non-dimensional function $f_2$, from (6.12), in (*b*), for the different cases in table 1: solid line, reference case A11; dashed line, case A21 with double $D$; dot-dashed line, case A12 with double $\chi_s$.

where the non-dimensional coefficients

$$c_\varepsilon = \frac{1}{w^{*3}} \int \varepsilon \, \mathrm{d}z, \qquad c_q = \frac{1}{w^{*2} z^*} \int q^2 \, \mathrm{d}z \tag{6.10}$$

are plotted in figure 14(*a*) as a function of time. The quantity $c_q$ must approach a constant behaviour $c_q(D, \chi_s)$ if the convection scales $w^*$ and $z^*$ really characterize the turbulent motion of the convection layer, and such a behaviour is approximately observed after an initial transient beyond $t(B_s/h^2)^{1/3} \simeq 5$, though there are still oscillations of the order of 10 % which are likely due to a lack of statistical convergence; wider domains would be necessary to assess this question. The approximately steady evolution of $c_\varepsilon(D, \chi_s)$ after the initial transient (also appreciated in figure 14(*a*)) represents the inviscid scaling of the turbulent dissipation rate.

If we accept this constancy of both coefficients, (6.9) and the definition $w^{*3} = B_s z^*$ provide a system of two equations for the two unknowns $w^*$ and $z^*$, which can be easily integrated. In particular, we can write

$$\frac{\mathrm{d}z^*}{\mathrm{d}t} = f_2 w^*, \tag{6.11}$$

where a second non-dimensional function $f_2(D, \chi_s)$ defined by

$$f_2 = \frac{6}{5} \frac{1 - c_\varepsilon}{c_q} \tag{6.12}$$

appears in the general description of the system, in addition to the function $f_1$ characterizing the inversion layer. Equation (6.11) explicitly gives the growth rate of the thickness of the convection layer $\mathrm{d}z^*/\mathrm{d}t$ in terms of the convection velocity $w^*$. Once an initial condition is provided, e.g. the thickness $z^*(t_1)$ at a particular time $t_1$, the depth of mixing region evolves according to

$$z^*(t) = z^*(t_1) \left[ 1 + (2 f_2/3) \frac{t - t_1}{[z^*(t_1)^2/B_s]^{1/3}} \right]^{3/2}. \tag{6.13}$$

We then need $f_2$. The evolution of $f_2$ is plotted in figure 14(*b*) for the three cases in table 1. These curves show more temporal variability than $f_1$ in figure 10, but it can also be concluded that, within the accuracy allowed by the statistical convergence

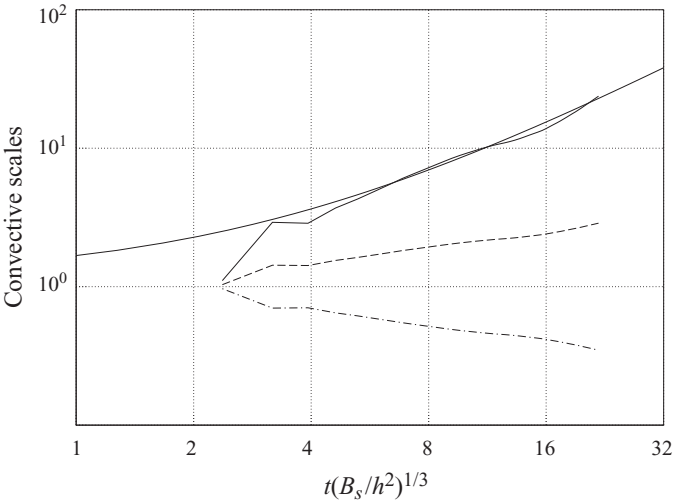


FIGURE 15. Temporal evolution of the convection scales in terms of the thickness $h$ of the inversion layer: solid line, length $z^*/h$; dashed line, velocity $w^*/(B_s h)^{1/3}$; dot-dashed line, buoyancy $b^*/(B_s^2/h)^{1/3}$; the smooth solid line corresponds to (6.13).

of the current simulations, they approach a constant value. It is also noted that the variation of $f_2$ with $D$ and $\chi_s$ is small, meaning that the main dependence of the statistics here considered on the buoyancy-reversal parameters is captured by the definition of the reference buoyancy flux $B_s$ given by (6.2). A mean value for each case constructed over the interval of time $t_1 < t < t_2$ is collected in table 1, and varies between 0.48 and 0.54. Once $f_2$ is known, (6.13) provides accurate predictions of the evolution in time of the depth $z^*$ of the convection layer. For instance, the mean value $f_2 \simeq 0.48$ was used for the reference case A11 and the result is shown in figure 15, comparing it with that computed from its definition (6.4). The difference between theory and results of about 10 % is consistent with the oscillations observed in figure 14. Once $z^*$ is available, a good prediction of the other convection scales follows immediately from their very definition because $B_s$ is a known constant. In particular, we have the power laws $w^* \propto t^{1/2}$ and $b^* \propto t^{-1/2}$; both of these variables are included in figure 15 as well.

A note on the time scales is worth the discussion at this point. Equation (6.13) indicates that the characteristic time of the turbulent convection zone is of the order of $(z^{*2}/B_s)^{1/3}$ (increasing with time as $z^*$ grows), and this is the reason to normalize the horizontal axis in figures 14 and 15 with $(h^2/B_s)^{1/3}$. This scale is different from that of the inversion layer, equal to $h^2/\kappa$ according to the discussion presented in § 5. The ratio of both time scales is $0.1 f_1(\chi_s \chi_c^2/Pr)^{1/3}(z^*/h)^{2/3}$, and this is a small number for the conditions considered here, of the order of 0.1 for the values $z^*/h \simeq 20$ reached in these simulations, which explains the difference in the magnitude of the non-dimensional times appearing in the figures of § 5 from those appearing in this section. The convection layer must become of the order of 600 times thicker than the inversion layer for both time scales to be comparable, and this number explains why, with the domain sizes affordable in this study, the inversion moves upwards extremely little compared to the growth of the turbulent region underneath.

This section can be summarized as follows: the state below the inversion base is analogous to free convection below a cold plate. Hence, an expression of the reference

| | $z^*/h$ | $\eta/\Delta x$ | $z^*/\lambda_z$ | $\lambda_z/\eta$ | $u'/w^*$ | $w'/w^*$ | $Re_t$ | $Re_\lambda$ | $Re^*$ | $Ri^*$ | $Ra^*$ |
|---|---|---|---|---|---|---|---|---|---|---|---|
| A11 | 24 | 1.2 | 19 | 28 | 0.84 | 0.74 | 1800 | 220 | 4800 | 590 | $0.4 \times 10^9$ |
| A21 | 39 | 0.9 | 26 | 31 | 0.86 | 0.78 | 2400 | 250 | 8000 | 293 | $1.1 \times 10^9$ |
| A12 | 39 | 1.2 | 19 | 28 | 0.90 | 0.76 | 1600 | 200 | 4800 | 716 | $0.5 \times 10^9$ |

TABLE 2. Length-scale ratios, turbulence intensities and derived quantities at the final time $t_2$. Reynolds numbers $Re_t = (q^2/2)^2/(\varepsilon\nu)$, $Re_\lambda = w'\lambda_z/\nu$ and $Re^* = z^* w^*/\nu$; convection Richardson number $Ri^* = b_1 z^*/w^{*2}$; Rayleigh number $Ra^* = z^{*3}|b_s|/(\kappa\nu)$; Nusselt number $Nu^* = w_e z^*/\kappa = z^*/h$. Maximum values are used for the mean turbulent dissipation rate $\varepsilon$ and the turbulence intensities.

buoyancy flux $B_s$ has been derived (cf. (6.2)), and the convection scales constructed from it characterize the statistics inside this turbulent region and allow the derivation of an explicit expression for the growth rate of the convection layer (cf. (6.13)).

## 7. Discussion

So far, we have tried to dissect the system analysing the different regions conforming it (sketched in figure 8) as independently as possible. The intention of this section is to bring them together and consider the problem as a whole, and we do it by looking at the system from different points of view.

### 7.1. *Turbulence parameters*

The turbulent state of the mixing layer can be characterized by the convection Reynolds number

$$Re^* = \frac{z^* w^*}{\nu}. \tag{7.1}$$

The values achieved at the end of the simulations vary between 5000 and 8000 depending on the case, which, although moderate, are high enough to explain the turbulent character of the flow. Note that it keeps increasing as $Re^* \propto t^2$ based on the scalings $z^* \propto t^{3/2}$ and $w^* \propto t^{1/2}$ obtained before. The Taylor-scale Reynolds number $Re_\lambda = w_{rms}\lambda_z/\nu$ based on the vertical fluctuations, where $\lambda_z = w_{rms}/[\langle(\partial w'/\partial z)^2\rangle]^{1/2}$ is the corresponding Taylor microscale, has been calculated using the statistical values at $\xi \simeq -0.4$, where the maximum of the vertical turbulent kinetic energy is found according to figure 12(*b*). The final values are above 200, relatively large. Note, however, that the flow is very anisotropic and, if the isotropic definition $[5q^4/(3\varepsilon\nu)]^{1/2}$ of the Taylor-scale Reynolds number is used, the magnitude is about 100.

Table 2 presents different scales and parameters characterizing the flow at the final time $t_2$, when the three cases have a similar thickness $z^*$ of the turbulent convection layer. It is observed that the buoyancy-reversal parameter $D$ has a greater effect than the saturation mixture fraction $\chi_s$, and simulation A21 shows a larger Reynolds number than the other two as a consequence of the corresponding more intense forcing. This behaviour is consistent with (6.2), which shows that the reference buoyancy flux $B_s$ depends more strongly on the saturation buoyancy anomaly $b_s$ than on $\chi_s$. However, the velocity r.m.s. normalized by $w^*$ is approximately the same in all three cases, which confirms the dominant role of this convection velocity in characterizing the turbulent region.

The Kolmogorov length $\eta = (\nu^3/\varepsilon)^{1/4}$ is included in table 2 in terms of the ratio to the Taylor microscale $\lambda_z$ to provide a measure of the scale separation, which is moderate,

of the order of 30. The ratio $\eta/\Delta x$ of order 1, which is comparable with values in other simulation studies using the same numerical algorithm, guarantees a good enough resolution. It is worth noting that the Kolmogorov scales remain constant in time, since $\varepsilon$ is proportional to $B_s = w^{*3}/z^*$ (see figure 13*a*), and this reference buoyancy flux is constant; the system develops self-similarly, generating increasingly larger scales. The ratio between the inversion thickness $h$ and the Kolmogorov scale $\eta$ is therefore constant and, for the reference case A11, it is relatively large, about 25.

### 7.2. *Classical turbulent convection*

As often mentioned previously, the cloud-top mixing layer presents certain similarities with free convection below a cold surface. In this respect, it is appropriate to define a Rayleigh number as

$$Ra^* = \frac{z^{*3}|b_s|}{\kappa\nu}, \tag{7.2}$$

based on the buoyancy anomaly $b_s$ at saturation conditions. It increases with time proportionally to $t^{9/2}$ as the convection layer thickens into the cloud, reaching values in the range $(0.5\text{–}1.0)\times10^9$ by the end of the simulations.

It is more difficult to define a surrogate for the thermal layer, because here the saturation surface $\chi(\boldsymbol{x}, t) = \chi_s$ at which the Dirichlet boundary condition $b = b_s$ is imposed is fluctuating. However, we have found in § 4 that this iso-surface remains close to the inversion base in comparison to the thickness $z^*$ of the convection layer – increasingly close as the system develops in time. At the same time, figure 5(*b*) clearly shows that the molecular flux of the mixture fraction falls for $z < z_i$ relatively fast over a thin region in favour of the turbulent flux. In sum, it seems reasonable to define a thermal boundary layer based on the mean gradient of $\chi$ evaluated at $z = z_i$, the inversion base. This yields $\chi_i\delta_\chi$ as the thickness of that thermal layer, i.e. a fraction $\chi_i/(1-\chi_i)$ (order 1) of the inversion layer thickness $h$, and therefore it also remains constant in time.

The Nusselt number can be defined as usual by the ratio between the actual molecular transport of the stratifying scalar $\chi$ through the inversion, quantified by $w_e$ in (6.1), and a reference one $\kappa/z^*$ based only on pure diffusion, i.e.

$$Nu^* = \frac{w_e z^*}{\kappa}. \tag{7.3}$$

Then, the Nusselt number is equal to the ratio between the depths of the turbulent layer, $z^*$, and of the inversion, $h = \kappa/w_e$; the values of this ratio at the end of the simulations are presented in table 2 and vary between 25 and 40.

Figure 16 uses $Ra^*$ as an independent variable instead of the time $t$ to plot different parameters. The convection Reynolds number introduced before can be expressed as $Re^* \propto (Ra^*)^{4/9}Pr^{-2/3}$ ($Pr = 1$ in our case) according to the definition of $B_s$ in (6.2), where the constant of proportionality is given by $(0.1 f_1 \chi_c^{2/3}/\chi_s)^{1/3}$. Similarly, the Nusselt and Rayleigh numbers are related by $Nu^* = (0.1 f_1 \chi_c^{2/3})(Ra^*)^{1/3}$. The good agreement between these scalings and the data (seen in figure 16), or equivalently, the constancy of the scaling exponents 4/9 for the Reynolds number and 1/3 for the Nusselt number, follows from the steadiness of the non-dimensional function $f_1$ shown in figure 10 (the normalized mean entrainment velocity $w_e$), and they are one of the possible limits reported in the literature (Turner 1973; Siggia 1994; Ahlers *et al.* 2009). It corresponds to the case of no mean wind, which is consistent with the situation here because the system is an open configuration and there is no external constraint (like the boundaries of a tank) that imposes a large-scale circulation.

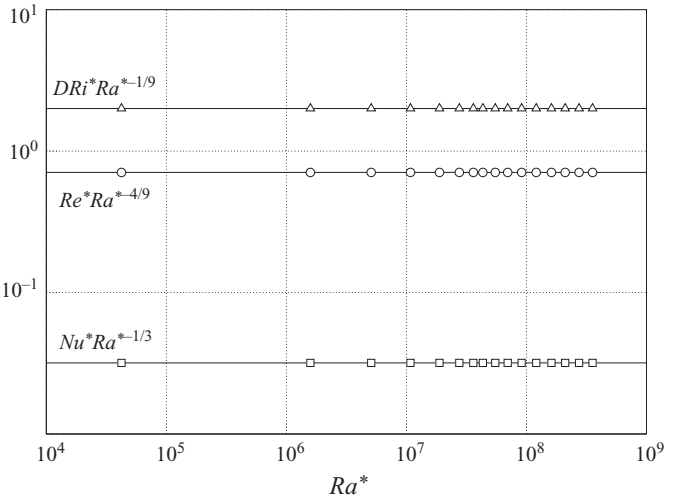


FIGURE 16. Non-dimensional parameters as a function of the Rayleigh number for reference case A11: circles, Reynolds number; squares, Nusselt number; triangles, Richardson number. Lines indicate the power-law scalings discussed in the text.

### 7.3. *Mixing across the density interface*

The vertical structure of the system, namely the fact that a turbulent mixing zone is established next to an inversion layer, makes the problem akin to that of turbulent mixing across a density interface (Turner 1973; Fernando 1991; Fernando & Hunt 1997). From this point of view, the convection Richardson number

$$Ri^* = \frac{b_1 z^*}{w^{*2}} \tag{7.4}$$

plays an important role and therefore it is also included in figure 16. The scaling as $DRi^* \propto (Ra^*)^{1/9} Pr^{1/9}$ observed in this figure, with the constant of proportionality equal to $(0.1 f_1 \chi_c^{2/3}/\chi_s)^{-2/3}$, is again a simple consequence of the steadiness of $f_1$. More relevant for this discussion is the high value that it reaches, of the order of 300 or larger and increasing with time as $t^{1/2}$. This result helps in explaining why the turbulence is not likely to break the inversion, as appreciated repeatedly during this study. Note that the gradient Richardson number corresponding to the strong horizontal motion observed in figure 12(*b*) just beneath the inversion base at $z = z_i$ leads to a similar conclusion because, although the magnitude of the velocity grows as $t^{1/2}$, the thickness of the transition layer over which this maximum horizontal velocity develops seems to be of the order of $0.1z^*$, i.e. it increases proportionally to $t^{3/2}$, and the associated shear strength diminishes with time while the stratification of the inversion remains constant.

A Richardson number $Ri_\eta = b_1 \eta / v_\eta^2$ based on the Kolmogorov scales, though smaller than $Ri^*$, still remains larger than 1. It can be shown that the definitions of $\eta$ and $v_\eta = (\nu\varepsilon)^{1/4}$, along with (6.2), lead to the relation $DRi_\eta \propto (B_s/\varepsilon)^{3/4} Pr^{1/4}$, where the constant of proportionality is $(0.1 f_1 \chi_c^{2/3}/\chi_s)^{-3/4}$. The scaling of the dissipation rate $\varepsilon$ with $B_s$ implies that the right-hand side is constant and of order unity for the cases of interest shown in table 1. Therefore, $Ri_\eta \sim 1/D$, and this estimate indicates that not even the smallest (in the average) turbulent scales can break the inversion and the turbulence is obliged to remain within the cloud, since $D \ll 1$ for the usual atmospheric conditions.

Another relevant parameter in this context is the internal Richardson number defined in terms of the inversion thickness $h$ by

$$Ri_{(I)} = \frac{b_1 h}{w^{*2}}. \tag{7.5}$$

Values below $\pi^2$ are associated with the flapping of a thin inversion, whereas the condition $Ri_{(I)} > \pi^2$ corresponds to a relatively thick inversion that contains a certain number of modes of internal motion (see Fernando & Hunt 1997 and references therein). In our case, it can be written as $Ri_{(I)} = Ri^* h/z^*$ and table 2 shows that $Ri_{(I)}$ varies between 10 and 25 among the different cases. This result implies the possibility of a wave motion inside the inversion that would explain the fluctuations observed in the scalar field (figure 7*b*) and the velocity field (figure 12) for $z > z_i$. On the other hand, these numbers are close to the cross-over value $\pi^2$ and $Ri_{(I)}$ diminishes with time as $t^{-1}$ due to the growth of the velocity $w^*$, which suggests that a change in regime, and maybe in scaling laws, could appear later in time. However, it is not clear how the formation of the reversing mixtures adjacent to the inversion (see figure 2), which are ultimately the driving mechanism of the whole system, could modify this behaviour. Larger domains are needed to investigate this issue.

It is also interesting to express the mean entrainment velocity $w_e$ as a function of the convection Richardson number $Ri^*$ defined above. Within the regime considered in this study, (6.2) leads to

$$\frac{w_e}{w^*} = \chi_s (DRi^*)^{-1}, \tag{7.6}$$

recovering one of the power-law scalings commonly proposed in the literature (Turner 1973; Fernando 1991; Sayler & Breidenthal 1998). It is worth noting that the ratio $w_e/w^*$ is very small, since $\chi_s \ll 1$ for normal atmospheric conditions and $DRi^* > 1$ increases with time, as discussed after (7.4), and it quantifies the observation often made before during this study that the turbulent convection layer broadens within the cloud very fast compared to the steady motion upwards of the inversion.

In sum, we have observed certain similarities between the cloud-top mixing layer and the classical problem of turbulent mixing across a density interface. However, in spite of these analogies, it should be kept in mind that the cloud-top mixing layer is driven by the local phenomena occurring at the density interface itself (buoyancy reversal resulting from molecular mixing) and the turbulent motion is a consequence of this. In this respect, the cloud top is different from the classical problem, where the turbulent state is imposed at some given distance from the inversion by some external mechanism (normally an oscillating grid or a mean shear). For this reason, the former coupled configuration as a whole has been denominated as interfacial convection in the past by Sayler & Breidenthal (1998), who considered radiative forcing in a closed tank instead of the evaporative cooling effects in an open domain studied in this paper.

### 7.4. *Stratocumulus top*

Last, the results need to be considered from the point of view of the atmospheric problem that motivated this investigation in the first place, namely the stratocumulus top. It is, however, important to recall that the focus of the current research is not the stratocumulus-topped boundary layer as a whole, but a small domain around the cloud upper boundary. In particular, the simulations discussed in this paper correspond to a thickness of $2z^* \simeq 5\,\mathrm{m}$ (the time interval is $t_2 \simeq 200$ s), a size that overlaps with the grid steps currently used in large-eddy simulations.

The first result to emphasize is that the buoyancy-reversal instability indeed leads to a turbulent state inside the cloud layer, but the inversion is not broken – there is no finger of pure upper layer fluid penetrating deep across the inversion into the lower region. The only consequence of the turbulent mixing that develops is that the inversion is forced to travel upwards at a constant speed $w_e$, instead of propagating at the usual diffusion rate proportional to $\sqrt{\kappa/t}$.

The second thing to comment on is that the scales associated with the cloud-top mixing layer driven purely by evaporative cooling are small. For instance, for the reference case A11 corresponding to field measurements during the flight RF01 of the DYCOMS-II campaign, $w_e = 0.1 f_1 (\kappa |b_s| \chi_c^2)^{1/3}$ is equal to $0.16\,\mathrm{mm\,s^{-1}}$, and the associated inversion thickness $h = \kappa / w_e$ is about 97 mm ($\kappa = 1.5 \times 10^{-5}\,\mathrm{m^2\,s^{-1}}$ and an inversion strength $b_1 = 0.25\,\mathrm{m\,s^{-2}}$ have been used in these estimates). The reference buoyancy flux $B_s = w_s |b_s| / \chi_s$ is then $1.3 \times 10^{-5}\,\mathrm{m^2\,s^{-3}}$. Using a thickness $2z^*$ of approximately 5 m implies a characteristic velocity fluctuation $w^* = (B_s z^*)^{1/3}$ of about $32\,\mathrm{mm\,s^{-1}}$ and the broadening velocity is $\mathrm{d}z^*/\mathrm{d}t = f_2 w^* \simeq 15\,\mathrm{mm\,s^{-1}}$. These values are at least one order of magnitude smaller than those encountered at the cloud top (Stevens *et al.* 2003*a*; Gerber *et al.* 2005), where entrainment rates $w_e$ vary between 3 and $5\,\mathrm{mm\,s^{-1}}$, velocity fluctuations are of the order of $1\,\mathrm{m\,s^{-1}}$ and turbulent dissipation rates about $10^{-2}\,\mathrm{m^2\,s^{-3}}$ are measured, and indicate that the entrainment mechanism is not determined by evaporative cooling alone, but by some of the other physical phenomena entering into the problem.

This conclusion is consistent with previous work, suggesting that evaporative cooling plays a minimal role at the cloud top even though buoyancy reversal is predicted to occur (Gerber *et al.* 2005). A different question is what is the role of evaporative cooling in the boundary of already existing holes created, for instance, by the radiatively driven convection, such as the cloud interior mixing instability proposed by Gerber *et al.* (2005) and further studied by Haman (2009). We cannot comment on these issues because all additional forcings apart from evaporative cooling have been eliminated in our simulations, and therefore the question remains open.

Third, it has been shown that the system is controlled by molecular processes at the inversion base. (The reference buoyancy flux $B_s$ depends explicitly on the scalar diffusivity $\kappa$.) This behaviour, in particular a mean entrainment rate proportional to $\kappa^{1/3}$, has already been proposed by Wunsch (2003), and it implies that models, e.g. subgrid closures for large-eddy simulations, need to retain the effect of molecular processes in them (which is not normally the case) if they are to faithfully capture the phenomena studied in this paper.

Further comparisons of the current results, based on direct numerical simulations of open configurations, with those of Wunsch (2003), based on stochastic simulations of closed configurations, are nevertheless limited. The solid wall at the bottom in the latter case possibly modifies the upward entrainment rate $w_e$ and certainly changes in time the mean value of the mixture fraction of the lower region when adiabatic boundary conditions are employed. Similarly, extrapolations of our study to higher values of $D$ require caution because the parallelism with free convection below a cold plate often employed in this paper was based on the observation that the saturation surface $\chi(\boldsymbol{x}, t) = \chi_s$ remains increasingly close to the inversion base, a horizontal reference plane; it is not clear what happens when $D \simeq 1$, i.e. when the time scale of the falling reversal mixtures is comparable to that of the restoring force of the inversion and therefore the saturation surface might become more convoluted. These issues remain to be explored in future work.

## 8. Conclusions

Latent-heat effects in the turbulent cloud-top mixing layer have been investigated for the typical atmospheric conditions of small buoyancy reversal $0 < D = -b_s/b_1 \ll 1$ using direct numerical simulations. It has been shown that the buoyancy-reversal instability leads to a turbulent state inside the cloud. However, results have also confirmed that these evaporative cooling effects do not break the inversion.

A regime is established with a vertical structure that consists of an inversion layer on top, dominated by molecular transport, and a turbulent convection layer below, dominated by turbulent transport. The separation of both is well represented by the position of the maximum mean buoyancy gradient (maximum mean stratification), the inversion base. It is shown that molecular processes at this inversion base determine the evolution of the whole system, which helps to explain the difficulties encountered in the past to study the problem using large-eddy simulation with classical subgrid closures.

The inversion layer is characterized by the inner scales formed with the constant upward mean entrainment velocity $w_e = 0.1 f_1(\kappa |b_s| \chi_c^2)^{1/3}$ (the Prandtl number is considered to be unity throughout this paper) and the diffusivity $\kappa$ of the stratifying scalar $\chi$, where $b_s$ is the buoyancy anomaly at saturation conditions $\chi_s$, and $\chi_c = (\chi_s + D)/(1 + D)$ is the interval of buoyancy reversing mixtures. In particular, this inversion layer has a constant depth $h = \kappa/w_e$. The non-dimensional function $f_1(D, \chi_s)$ is of order 1, and remains approximately constant in the interval of small parameters $D$ and $\chi_s$ characteristic of atmospheric conditions at the stratocumulus top. The evolution of this region is negligibly slow compared to the rate at which the convection layer below deepens into the cloud, making the problem similar to that of free convection below a quasi-stationary cold plate.

The turbulent convection layer inside the cloud is characterized by the outer or convection scales constructed with the reference buoyancy flux $B_s = |b_s| w_e/\chi_s$ and the length scale $z^* = \int B \, \mathrm{d}z/B_s$ obtained from the depth-integrated turbulent buoyancy flux $B = \langle w'b' \rangle$. A self-preserving state is approached where the thickness of the turbulent region, of order $2z^*$, grows according to $z^* \simeq [(2f_2/3)^3 B_s t^3]^{1/2}$, the velocity scales with $w^* = (B_s z^*)^{1/3}$ and the buoyancy fluctuation is of the order of $b^* = B_s/w^* = (B_s^2/z^*)^{1/3}$. The non-dimensional function $f_2(D, \chi_s)$ is also of order 1 and approximately independent of the buoyancy-reversal parameters within the range of interest.

The Reynolds number $z^* w^*/\nu$ achieved in the simulations varies between 5000 and 8000, depending on the case. The corresponding Rayleigh number $z^{*3}|b_s|/(\nu\kappa)$ is within the interval $(0.5\text{–}1.0) \times 10^9$, and the Nusselt number $w_e z^*/\kappa$ varies between 25 and 40. The Reynolds and Nusselt numbers show power-law dependencies on the Rayleigh number with exponents 4/9 and 1/3, which correspond to the classical limit of no mean wind reported in free-convection problems. The convection Richardson number $b_1 z^*/w^{*2}$ is larger than 300 and increases with time, which explains the inability of the turbulent layer to penetrate through the capping inversion.

The upper part of the convection layer, a transition or buffer zone of approximate thickness $0.1z^*$, is dynamically very active, with a strong transfer of vertical to horizontal motion that brings about an intense anisotropy in the flow. This entails the formation of a planform cellular pattern and sheet-like plumes, in agreement with observations and laboratory experiments of related problems. The saturation surface (instantaneous cloud top) lies predominantly inside this zone and is asymptotically close to the inversion base, and so is the minimum mean buoyancy.

| | Grid | $\delta_s/\chi_s$ | $\lvert\nabla\cdot\boldsymbol{v}\rvert_2/\lvert\nabla\times\boldsymbol{v}\rvert_2$ | $\Delta w_e$ (% ) |
|---|---|---|---|---|
| R1 | $1024\times1024\times\ 738$ | 1/16 | $2\times10^{-5}$ | – |
| R2 | $1024\times1024\times\ 738$ | 1/32 | $3\times10^{-5}$ | $0.8\pm1.9$ |
| R3 | $2048\times2048\times1536$ | 1/32 | $2\times10^{-6}$ | $0.6\pm1.9$ |
| R4 | $1024\times1024\times1024$ | 1/16 | $2\times10^{-5}$ | $0.4\pm1.8$ |

TABLE 3. Resolution requirements. Physical parameters $D$ and $\chi_s$ correspond to reference case A11 in table 1 and the reference Rayleigh number is $Ra=b_1L_0^3/(\nu\kappa)=10^{11}$. Dilatation error and the variation in the mean entrainment velocity (mean plus standard deviation) are shown in the last two columns.

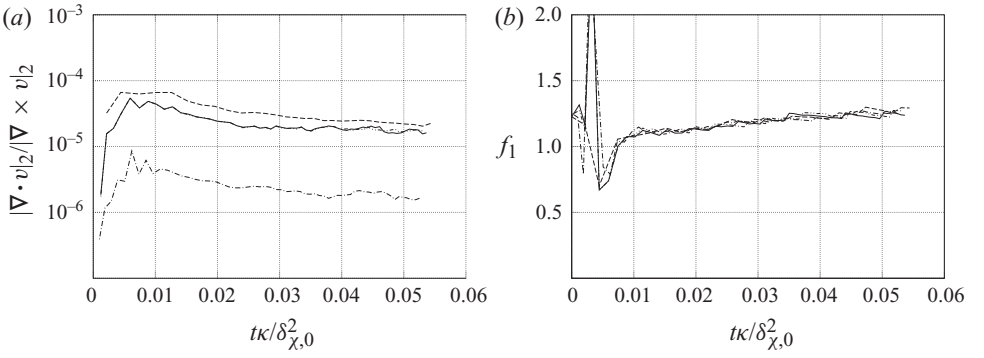


FIGURE 17. Resolution study: solid line, reference case R1; dashed line, modified case R2 with half $\delta_s$; dot-dashed line, modified case R3 with half $\Delta x$ (double number of grid points in each direction); dot-dot-dashed line, modified case R4 with $0.25L_0$ longer domain in the vertical direction.

Comments on the original manuscript by Professor B. Stevens and Professor H. Schmidt are gratefully acknowledged. Financial support for this work was provided by the Deutsche Forschungsgemeinschaft within the SPP 1276 Metström program. Computational time was provided by the German High Performance Computing Centre for Climate- and Earth System Research (DKRZ) in Hamburg.

## Appendix. Resolution requirements

Table 3 contains the set of simulations performed to confirm the independence of the results discussed in the paper with respect to several parameters that need to be prescribed in the simulation. The first case R1 corresponds to A11 in table 1 but with a smaller reference Rayleigh number $Ra=b_1L_0^3/(\nu\kappa)=10^{11}$, so that a smaller grid size can be employed. This case is used as a reference to study in R2 the influence of the smoothing parameter $\delta_s$ entering in the definition of the buoyancy mixing function $b^e(\chi)$ in (2.2). This simulation is employed in turn to investigate the influence of the resolution in case R3 by varying the grid step $\Delta x$. Last, the effect of the domain size is considered in simulation R4. The rest of the parameters are kept the same in all four cases.

The effect of $\delta_s$ is considered first. The residual dilatation, which represents part of the numerical error of the algorithm (Mellado *et al.* 2010), is plotted in figure 17(*a*) in terms of the $L_2$-norm. First, it is observed that the magnitude of this error is very

small compared to other quantities associated with the velocity-gradient tensor, such as in the case of the enstrophy shown in figure 17($a$). Second, when the smoothing parameter is reduced, there is an increase of about a factor 2, but this relative error remains small during the whole simulation, below $10^{-4}$. Visualizations of the dilatation (not shown) indicate that this error concentrates at the inversion base and at the front of the falling downdrafts, where the steepest gradients form. On the other hand, the effect on quantities of interest is small. For instance, figure 17($b$) shows the temporal evolution of the mean entrainment velocity $w_e$, as in figure 10, whose importance in the development of the system has been clearly exposed in the main text. It is appreciated that the deviation of R2 with respect to R1 is small; the last column of table 3 quantifies this variation with respect to the reference case R1 in terms of the mean and standard deviation of the relative difference in $w_e$ along the simulation, and it is less than 3 %. It is clear that other quantities do indeed depend on $\delta_s$, for instance the pointwise maximum of the buoyancy gradient because of the very definition of $b^e(\chi)$, but this study does not focus on them.

Simulation R3, with a grid size $2048 \times 2048 \times 1536$, was performed interpolating the same initial condition as in case R1 into this new grid. The grid step $\Delta x$ is therefore half of that in R2, the rest of the conditions being equal. The same two statistics as used before to study the effect of $\delta_s$ are represented in figure 17 for this new simulation. The residual dilatation decreases by an order of magnitude because of the increase in resolution, but the relevant large-scale statistics remain close to the reference case R1, as observed in the evolution of $w_e$.

Finally, case R4 explores the influence of the size of the vertical domain by augmenting it in a length $0.25L_0$, where $L_0$ is the horizontal dimension of the computational domain. Recall that we need to place the upper and lower boundaries far enough from the turbulent mixing zone to avoid any influence of the particular boundary conditions imposed on the system, since we are interested in the open-domain configuration, but at the same time computational cost needs to be minimized. Comparisons between simulations R1 and R4 in figure 17 again confirm that the reference case R1 is well defined in this respect. The value of the pressure fluctuation intensity at the upper and lower boundaries at the final time is about 3 % of the magnitude in the core of the turbulent region. The inversion base is at a distance of about $0.25L_0$ from the upper boundary.

The conclusion of these resolution studies is that case R1 is well resolved, and gives a reference for the scaling of the problem based on the results presented throughout this paper, i.e. what grid size is needed for a given diffusivity $\kappa$. In particular, during the bulk of the simulation R1, the resolution measured in terms of the inversion thickens is $\delta_\chi/\Delta x \simeq 32$, in terms of a reference buoyancy-reversal layer is $\chi_c\delta_\chi/\Delta x \simeq 3.8$ and in terms of the Kolmogorov scale is $\eta/\Delta x \simeq 0.6$.

## REFERENCES

Adrian, R. J., Ferreira, R. T. D. S. & Boberg, T. 1986 Turbulent thermal convection in wide horizontal layers. *Exp. Fluids* **4**, 121–141.

Ahlers, G., Grossmann, S. & Lohse, D. 2009 Heat transfer and large scale dynamics in turbulent Rayleigh–Bénard convection. *Rev. Mod. Phys.* **81**, 503–537.

Albrecht, B. A., Penc, R. S. & Schubert, W. H. 1985 An observational study of cloud-topped mixed layers. *J. Atmos. Sci.* **42**, 800–822.

Asaeda, T. & Watanabe, K. 1989 The mechanism of heat transport in thermal convection at high Rayleigh numbers. *Phys. Fluids* A **1** (5), 861–867.

Bretherton, C. S. 1987 A theory for nonprecipitating moist convection between two parallel plates. Part 1. Thermodynamics and linear solutions. *J. Atmos. Sci.* **44**, 1809–1827.

Caughey, S. J., Crease, B. A. & Roach, W. T. 1982 A field study of nocturnal stratocumulus. Part 2. Turbulence structure and entrainment. *Q. J. R. Meteorol. Soc.* **108**, 125–144.

Deardorff, J. W. 1970 Convective velocity and temperature scales for the unstable planetary boundary layer and for Rayleigh convection. *J. Atmos. Sci.* **27**, 1211–1213.

Deardorff, J. W. 1980 Cloud top entrainment instability. *J. Atmos. Sci.* **37**, 131–147.

Deardorff, J. W. & Willis, G. E. 1967 Investigation of turbulent thermal convection between horizontal plates. *J. Fluid Mech.* **28**, 675–704.

Faloona, I., Lenschow, D. H., Campos, T., Stevens, B., van Zanten, M., Bloomquist, B., Thorton, D., Bandy, A. & Gerber, H. 2005 Observations of entrainment in eastern Pacific marine stratocumulus using three conserved scalars. *J. Atmos. Sci.* **62**, 3268–3284.

Fernando, H. J. S. 1991 Turbulent mixing in stratified fluids. *Annu. Rev. Fluid Mech.* **23**, 455–493.

Fernando, H. J. S. & Hunt, J. C. R. 1997 Turbulence, waves and mixing at shear-free density interfaces. Part 1. A theoretical model. *J. Fluid Mech.* **347**, 197–234.

Flack, K. A., Saylor, J. R. & Smith, G. B. 2001 Near-surface turbulence for evaporative convection at an air/water interface. *Phys. Fluids* **13** (11), 3338–3345.

Gerber, H., Malinowski, G., Frick S. P., Brenguier, J.-L. & Burnet, F. 2005 Holes and entrainment in stratocumulus. *J. Atmos. Sci.* **62**, 443–459.

Goldstein, R. J. & Volino, R. J. 1995 Onset and development of natural convection above a suddenly heated horizontal surface. *J. Heat Transfer* **117**, 884–894.

Haman, K. E. 2009 Simple approach to dynamics of entrainment interface layers and cloud holes in stratocumulus clouds. *Q. J. R. Meteorol. Soc.* **135**, 93–100.

Haman, K. E., Malinowski, S. P., Kurowski, M. J., Gerber, H. & Brenguier, J.-L. 2007 Small-scale mixing processes at the top of a marine stratocumulus: a case study. *Q. J. R. Meteorol. Soc.* **133**, 213–226.

Kerr, R. M. 2001 Energy budget in Rayleigh–Bénard convection. *Phys. Rev. Lett.* **87**, 244502.

Krueger, S. K. 1993 Linear eddy modeling of entrainment and mixing in stratus clouds. *J. Atmos. Sci.* **50**, 3078–3090.

Kunnen, R. P. J., Geurts, B. J. & Clercx, H. J. H. 2009 Turbulence statistics and energy budget in rotating Rayleigh–Bénard convection. *Eur. J. Mech.* B *Fluids* **28**, 578–589.

Kurowski, M. J., Malinowski, S. P. & Grabowski, W. 2009 A numerical investigation of entrainment and transport within a stratocumulus-topped boundary layer. *Q. J. R. Meteorol. Soc.* **135**, 77–92.

Leighton, R. I., Smith, G. B. & Handler, R. A. 2003 Direct numerical simulation of free convection beneath an air–water interface at low Rayleigh numbers. *Phys. Fluids* **15** (10), 3181–3193.

Lilly, D. K. 1968 Models of cloud-topped mixed layers under strong inversion. *Q. J. R. Meteorol. Soc.* **94**, 292–309.

Mellado, J. P., Stevens, B., Schmidt, H. & Peters, N. 2009 Buoyancy reversal in cloud-top mixing layers. *Q. J. R. Meteorol. Soc.* **135**, 963–978.

Mellado, J. P., Stevens, B., Schmidt, H. & Peters, N. 2010 Two-fluid formulation of the cloud-top mixing layer for direct numerical simulation. *Theor. Comput. Fluid Dyn.*, doi:10.1007/s00162-010-0182-x.

Moeng, C.-H. & Rotunno, R. 1990 Vertical velocity skewness in the bouyancy-driven boundary layer. *J. Atmos. Sci.* **47**, 1149–1162.

Moeng, C.-H., Stevens, B. & Sullivan, P. P. 2005 Where is the interface of the stratocumulus-topped PBL. *J. Atmos. Sci.* **62**, 2626–2631.

Nicholls, S. 1989 The structure of radiatively driven convection in stratocumulus. *Q. J. R. Meteorol. Soc.* **115**, 487–511.

Randall, D. A. 1980 Conditional instability of the first kind upside-down. *J. Atmos. Sci.* **37**, 125–130.

Sayler, B. J. & Breidenthal, R. E. 1998 Laboratory simulations of radiatively induced entrainment in stratiform clouds. *J. Geophys. Res.* **103** (D8), 8827–8837.

Shy, S. S. & Breidenthal, R. E. 1990 Laboratory experiments on the cloud-top entrainment instability. *J. Fluid Mech.* **214**, 1–15.

Siems, S. T. & Bretherton, C. S. 1992 A numerical investigation of cloud-top entrainment instability and related experiments. *Q. J. R. Meteorol. Soc.* **118**, 787–818.

Siems, S. T., Bretherton, C. S., Baker, M. B., Shy, S. & Breidenthal, R. E. 1990 Buoyancy reversal and cloud-top entrainment instability. *Q. J. R. Meteorol. Soc.* **116**, 705–739.

Siggia, E. D. 1994 High Rayleigh number convection. *Annu. Rev. Fluid Mech.* **26**, 137–168.

Stevens, B. 2002 Entrainment in stratocumulus-topped mixed layers. *Q. J. R. Meteorol. Soc.* **128**, 2663–2690.

Stevens, B., Lenschow, D. H., Faloona, I., Moeng, C.-H., Lilly, D. K., Blomquist, B., Vali, G., Bandy, A., Campos, T., Gerber, H., Haimov, S., Morley, B. & Thorton, C. 2003*a* On entrainment rates in nocturnal marine stratocumulus. *Q. J. R. Meteorol. Soc.* **129** (595), 3469–3493.

Stevens, B., Lenschow, D. H., Vali, G., Gerber, H., Bandy, A., Blomquist, B., Brenguier, J.-L., Bretherton, C. S., Burnet, F., Campos, T., Chai, S., Faloona, I., Friesen, D., Haimov, S., Laursen, K., Lilly, D. K., Loehrer, S. M., Malinowski, S. P., Morley, B., Petters, M. D., Rogers, D. C., Russel, L., Savic-Jovcic, V., Snider, J. R., Straub, D., Szumowski, M. J., Takagi, H., Thornton, D. C., Tschudi, M., Towhy, C., Wetzel, M. & van Zanten, M. C. 2003*b* Dynamics and chemistry of marine stratocumulus: DYCOMS-II. *Bull. Am. Meteorol. Soc.* **84**, 579–593.

Stevens, B., Moeng, C.-H., Ackerman, A. S., Bretherton, C. S., Chlond, A., de Roode, S., Edwards, J., Golaz, J.-C., Jiang, H., Khairoutdinov, M., Kirkpatrick, M. P., Lewellen, D. C., Lock, A., Müller, F., Stevens, D. E., Whelan, E. & Zhu, P. 2005 Evaluation of large-eddy simulations via observations of nocturnal marine stratocumulus. *Mon. Weather Rev.* **133**, 1443–1462.

Stevens, D. E., Bell, J. B., Almgren, A. S., Beckner, V. E. & Rendleman, C. A. 2000 Small-scale processes and entrainment in a stratocumulus marine boundary layer. *J. Atmos. Sci.* **57**, 567–581.

Sullivan, P. P., Moeng, C.-H., Stevens, B., Lenschow, D. H. & Mayor, S. D. 1998 Structure of the entrainment zone capping the convective atmospheric boundary layer. *J. Atmos. Sci.* **55**, 3042–3064.

Theerthan, S. A. & Arakeri, J. H. 2000 Planform structure and heat transfer in turbulent free convection over horizontal surfaces. *Phys. Fluids* **12** (4), 884–894.

Townsend, A. A. 1959 Temperature fluctuations over a heated horizontal surface. *J. Fluid Mech.* **5**, 209–241.

Turner, J. S. 1973 *Buoyancy Effects in Fluids*. Cambridge University Press.

Wunsch, S. 2003 Stochastic simulations of buoyancy reversal experiments. *Phys. Fluids* **15** (6), 1442–1456.

Yamaguchi, T. & Randall, D. A. 2008 Large-eddy simulation of evaporatively driven entrainment in cloud-topped mixed layers. *J. Atmos. Sci.* **65**, 1481–1504.